

Deriving three-dimensional properties of fracture networks from two-dimensional observations in rocks approaching failure under triaxial compression: Implications for fluid flow

Jessica McBeck¹ and François Renard²

¹University of Oslo

²The Njord Centre, Departments of Geosciences and Physics

November 24, 2022

Abstract

Approximating the three-dimensional structure of a fault network at depth in the subsurface is key for robust estimates of fluid flow. However, only observations of two-dimensional outcrops are often available. To shed light on the relationship between two- and three-dimensional measurements of fracture networks, we examine data from a unique set of eleven X-ray synchrotron triaxial compression experiments that reveal the evolving three-dimensional fracture network throughout loading. Using machine learning, we derive relationships between the two- and three-dimensional measurements of three properties that control fluid flow: the porosity, and volume and tortuosity of the largest fracture at a particular differential stress step. The models predict the porosity and volume of the largest fracture with R^2 scores of >0.99 , but predict the tortuosity with maximum R^2 scores of 0.68. To test the assumption that different rock types may require different equations between the two- and three-dimensional properties, we develop models for both individual rock types (granite, monzonite, marble, sandstone) and all of the experiments. Models developed using all of the experiments perform better than models developed for individual rock types, suggesting fundamental similarities between fracture networks in rocks often analyzed separately. Models developed with several parallel two-dimensional observations perform similarly to models developed with several perpendicular two-dimensional observations. When the models are developed with statistics of the two-dimensional observations, the models primarily depend on the mean and median when they predict the porosity, and minimum when they predict the volume and tortuosity.

1 **Deriving three-dimensional properties of fracture networks from two-dimensional**
2 **observations in rocks approaching failure under triaxial compression: Implications**
3 **for fluid flow**

4 **J. McBeck¹ and F. Renard^{1,2}**

5 ¹The Njord Centre, Departments of Geosciences and Physics, University of Oslo, Oslo, Norway.

6 ²ISTerre, Univ. Grenoble Alpes, Grenoble INP, Univ. Savoie Mont Blanc, CNRS, IRD, Univ.
7 Gustave Eiffel, 38000, Grenoble, France.

8 Corresponding author: Jess McBeck (j.a.mcbeck@geo.uio.no)

9 **Key Points:**

- 10 • Machine learning predicts three-dimensional fracture properties from two-dimensional
11 measurements.
- 12 • Model performance does not depend on the orientation of the two-dimensional
13 observations relative to the maximum compression direction.
- 14 • Models developed with several rock types perform better than models developed from
15 individual rock types.

16 **Abstract**

17 Approximating the three-dimensional structure of a fault network at depth in the subsurface is
18 key for robust estimates of fluid flow. However, only observations of two-dimensional outcrops
19 are often available. To shed light on the relationship between two- and three-dimensional
20 measurements of fracture networks, we examine data from a unique set of eleven X-ray
21 synchrotron triaxial compression experiments that reveal the evolving three-dimensional fracture
22 network throughout loading. Using machine learning, we derive relationships between the two-
23 and three-dimensional measurements of three properties that control fluid flow: the porosity, and
24 volume and tortuosity of the largest fracture at a particular differential stress step. The models
25 predict the porosity and volume of the largest fracture with R^2 scores of >0.99 , but predict the
26 tortuosity with maximum R^2 scores of 0.68. To test the assumption that different rock types may
27 require different equations between the two- and three-dimensional properties, we develop
28 models for both individual rock types (granite, monzonite, marble, sandstone) and all of the
29 experiments. Models developed using all of the experiments perform better than models
30 developed for individual rock types, suggesting fundamental similarities between fracture
31 networks in rocks often analyzed separately. Models developed with several parallel two-
32 dimensional observations perform similarly to models developed with several perpendicular two-
33 dimensional observations. When the models are developed with statistics of the two-dimensional
34 observations, the models primarily depend on the mean and median when they predict the
35 porosity, and minimum when they predict the volume and tortuosity.

36 **Plain Language Summary**

37 A fundamental problem in geoscience is extrapolating two-dimensional observations to three-
38 dimensional systems. For example, we may directly observe the length and width of a fracture
39 where it intersects the Earth's surface. Occasionally we may be able to find multiple two-
40 dimensional observations of the same fracture network. Attempts to simulate three-dimensional
41 fluid flow using two-dimensional systems have provided incorrect estimates of the true
42 permeability. Thus, to estimate the dynamics of fluid flow through a fault network we must
43 interpolate and/or extrapolate from two-dimensional observations to approximations of three-
44 dimensional systems. Here, we use machine learning to estimate three-dimensional
45 characteristics of fracture networks that control fluid flow from two-dimensional observations. In
46 situ X-ray tomography triaxial compression experiments provide unparalleled access to both the
47 three- and two-dimensional observations as the rock experiences increasing differential stress,
48 and develops more fractures. The work provides insight into the fundamental similarities
49 between fracture network development in different rock types, into the feasibility of developing
50 equations between two- and three-dimensional properties that control fluid flow, and into the
51 statistics of the two-dimensional property that are most beneficial to predicting the three-
52 dimensional properties.

53 **Keywords:** fracture network; fluid flow; triaxial compression; granite; sandstone; machine
54 learning

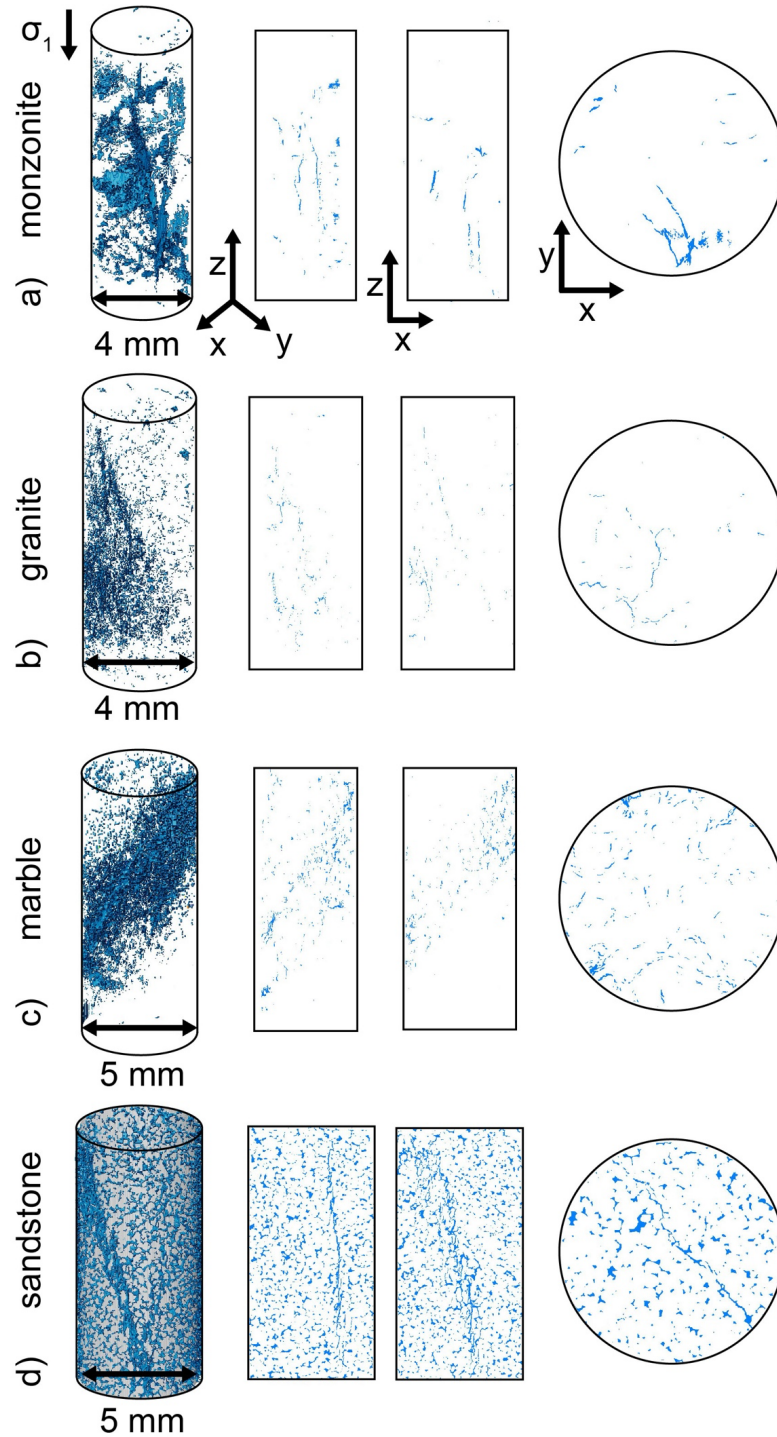
55 **1 Introduction**

56 Estimating characteristics of the three-dimensional structure of a tectonic system or fault
57 network from sparse, two-dimensional data is a key aspect of many field analyses (e.g., Moore et
58 al., 1990; Gueting et al., 2018), scaled physical experiments (e.g., Sassi et al., 1993; Dominguez

59 et al., 2000; Tong et al., 2014), and laboratory deformation experiments (e.g., Bobet & Einstein,
60 1998; Cao et al., 2020). Constraining the geometry of fracture networks in three-dimensions in
61 the subsurface is critical to robust assessments of seismic hazard (e.g., Kozłowska et al., 2018),
62 fluid flow (e.g., Auradou et al., 2005), and thus potential for CO₂ storage (e.g., Iding & Ringrose,
63 2010; Luhmann et al., 2017). However, the process of reconstructing three-dimensional fracture
64 geometries from two-dimensional data is often qualitative, and rarely formalized with
65 benchmarks to assess the accuracy of such reconstructions (e.g., Caumon et al., 2009; Lei et al.,
66 2017).

67 To reconstruct three-dimensional data from two-dimensional measurements, previous
68 analyses have relied on serial sectioning (e.g., Wei et al., 2019) and sub-sampling two-
69 dimensional slices (Karimpouli & Tahmasebi, 2016). Other analyses have used analytical and
70 statistical methods to estimate three-dimensional values (e.g., Roberts et al., 1997; Yeong &
71 Torquato, 1998; Manwart & Hilfer, 1999; Keehm et al., 2004; Lei et al., 2015; Saxena & Mavko,
72 2016). Such statistical methods measure properties, such as porosity, in two-dimensional images,
73 and then generate three-dimensional systems so that the statistics of the given property (e.g.,
74 porosity) match the measured three-dimensional statistics. While these methods can provide
75 reasonable estimates of some properties, they struggle to accurately capture the connectivity of
76 pore and fracture networks in three-dimensions (Hazlett, 1997; Manwart et al., 2000; Øren &
77 Bakke, 2002). Process-based reconstruction provides an alternative method of reconstruction that
78 can more closely approximate the connectivity of the pore network in sandstone than statistical
79 reconstruction (e.g., Bakke & Øren, 1997; Øren & Bakke, 2002). However, this method
80 simulates the packing of grains and subsequent processes, such as compaction and diagenesis,
81 that produce sandstones, for example, and thus cannot be applied to rocks that do not form with
82 this process, such as granite (e.g., Dong & Blunt, 2009).

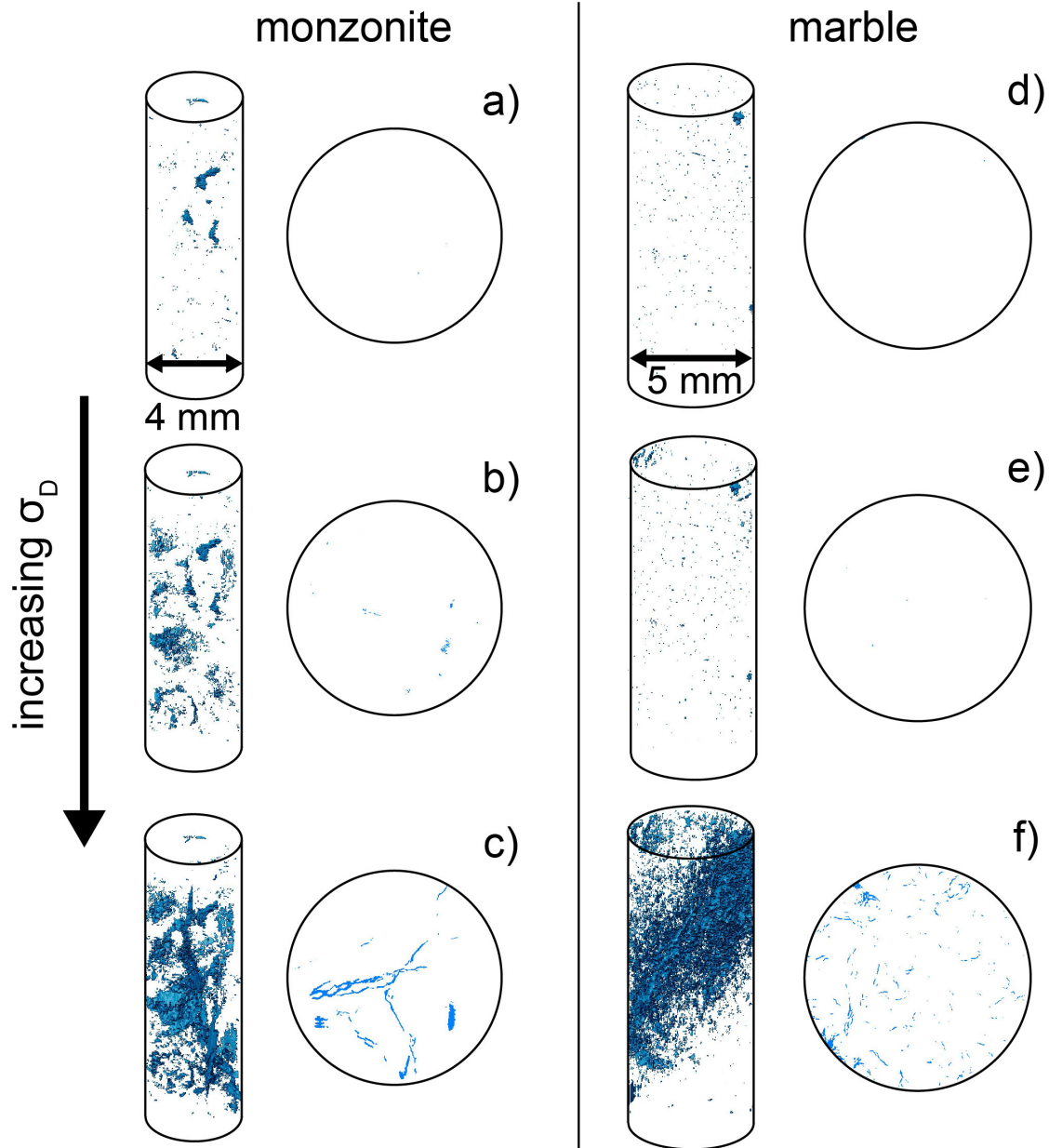
83 Due to the importance of fracture networks on fluid flow, recent studies have used
84 machine learning to predict the permeability of synthetic porous media (Tian et al., 2020; Santos
85 et al., 2020), and of natural rock cores, including sandstone, carbonate, and limestone (Sudakov
86 et al., 2019; Kamrava et al., 2020; Elmorsy et al., 2022). This work has produced models that can
87 predict the permeability of granular, porous rocks with strong positive correlations between the
88 measured and predicted permeability. However, this work did not attempt to predict the
89 permeability of rocks with more heterogeneous fracture networks, such as granite. It may be
90 more difficult to estimate the permeability of rocks that contain more heterogeneous fracture
91 networks, with a wider range of fracture lengths and spacing between fractures, than more
92 homogeneous rocks. Moreover, previous work focused on nominally intact rocks, rather than
93 rocks that had undergone some differential stress loading. In the field, the volumes of crust with
94 the largest permeabilities may tend to be those that experienced some inelastic deformation, such
95 as the highly fractured damage zone adjacent to the principal slip zone of faults (e.g., Mitchell &
96 Faulkner, 2012). Consequently, estimating the permeability of volumes of the crust with fracture
97 networks that developed due to increasing differential stress is critical for robust predictions of
98 fluid flow.



99

100 **Figure 1.** Example images of the fracture and pore networks in three-dimensional volumes (first
 101 column), two-dimensional vertical slices (second and third columns), and two-dimensional
 102 horizontal slices (fourth column) in four experiments: a) monzonite #5, b) granite
 103 #2, and c) marble #2, and d) sandstone #2. These scans were acquired immediately preceding macroscopic failure,
 104 after the initially intact rock was loaded to failure. The key goal of the present study is to predict
 105 the three-dimensional properties of fracture networks from two-dimensional observations.

106 In order to shed light on the relationships between two- and three-dimensional
107 measurements of the fracture networks within homogeneous and heterogeneous rocks subjected
108 to increasing differential stress, we examine data from eleven synchrotron X-ray
109 microtomography triaxial compression experiments performed on Fontainebleau sandstone,
110 Westerly granite, quartz monzonite, and Carrara marble (**Figure 1**). This data set is perhaps the
111 most comprehensive accumulation of two- and three-dimensional observations of fracture
112 networks that developed during triaxial compression deformation experiments with a wide range
113 of rock types. In these experiments, we systematically increase the differential stress on the rock
114 cores until the rocks fail, and acquire X-ray tomograms (i.e., scans) after each increase of
115 differential stress (**Figure 2**). We derive relationships between the two- and three-dimensional
116 measurements of three properties that control the fluid flow: the porosity, and the volume and
117 tortuosity of the largest fracture in the network at a particular differential stress step. We build
118 these relationships using two machine learning algorithms: gradient boosting and linear
119 regression. In order to constrain the feasibility of deriving an equation between these two- and
120 three-dimensional properties, we compare the ability of the machine learning models to predict
121 their values. We systematically examine how much data (e.g., number of two-dimensional slices)
122 is required to make accurate estimates of the three-dimensional property, and whether the
123 orientation of the two-dimensional slices controls the model success. Comparing the
124 performance of the models developed with slices of various orientations sheds light on the most
125 appropriate orientation of thin-sections in natural rock cores with varying mechanical structures,
126 including low porosity crystalline rocks and porous granular rocks, and the best type of two-
127 dimensional observations to gather in the field. We develop models for both individual rock
128 types (granite, monzonite, marble, and sandstone) and all of the experiments combined in order
129 to test the assumption that different rock types may require different equations between the two-
130 and three-dimensional property. We then develop models using the statistics of sets of two-
131 dimensional observations in order to identify the statistics that may be the most useful when
132 predicting the three-dimensional property. This work thus provides insight into 1) the
133 predictability of different fracture network properties, 2) the amount and type of data required for
134 successful estimates, and 3) the similarities of the relationships between two- and three-
135 dimensional properties in different rock types.



136

137 **Figure 2.** Example images of the three-dimensional and two-dimensional fracture networks from
 138 early in loading until immediately preceding macroscopic failure in two experiments: monzonite
 139 #5 (a-c), and marble #2 (d-f). The differential stress acting on the rocks, σ_D , increases from the
 140 top to the bottom of the figure.

141 2 Methods

142 2.1 Experimental conditions

143 We performed eleven triaxial compression experiments at beamline ID19 at the European
 144 Synchrotron and Radiation Facility, Grenoble, France. In these experiments, we insert one 10

145 mm tall and 4-5 mm diameter cylinder rock core in the Hades triaxial compression apparatus
 146 (Renard et al., 2016) installed on the beamline. The rock cylinders have different diameters so
 147 that the cores fail before the applied axial stress reaches the limit of the Hades apparatus (200
 148 MPa for 5 mm diameter samples, and 312 MPa for 4 mm diameter samples). We then impose a
 149 confining stress (5-35 MPa) using pressurized oil against the jacket surrounding each core
 150 sample (**Table 1**), and increase the axial stress in steps of 0.5-5 MPa, with smaller steps closer to
 151 failure, until the rock fails in a sudden stress drop (**Figure S1**), at ambient temperature
 152 conditions. After each increase in axial stress, we acquire an X-ray scan within 1.5 minutes while
 153 the rock is under load inside the Hades apparatus. Thus, the total number of X-ray scans acquired
 154 in an experiment depends on the chosen set of axial stress steps, and the stress conditions at
 155 which a rock fails, producing 38-136 scans for a given experiment (**Table 1**).

156 We deformed four rock types: Westerly granite, quartz monzonite, Carrara marble, and
 157 Fontainebleau sandstone. We analyze the relationship between the two- and three-dimensional
 158 properties of the fracture networks of these rocks because they represent endmembers of fracture
 159 network properties. Westerly granite and monzonite are low-porosity crystalline rocks dominated
 160 by interlocking quartz, feldspar, and mica crystals. The initial porosity of the monzonite and
 161 granite is lower than 1%. Carrara marble is a low porosity metamorphic rock that consists of
 162 calcite grains. Carrara marble has an initial porosity of about 0.2%, and grain sizes from 100-200
 163 μm (e.g., Rutter, 1972; Malaga-Starzec et al., 2002). Fontainebleau sandstone is comprised of
 164 cemented quartz grains. These Fontainebleau sandstone cores have a mean grain size of 250 μm
 165 and higher initial porosity than the marble: 5.5-7% (measured using the X-ray tomography
 166 images), and $6\pm 1\%$ (measured using imbibition with water) (Renard et al., 2018).

167

Experiment	Core diameter (mm)	Confining stress (MPa)	Number of scans	Experiment abbreviation
Westerly granite #1	4	5	38	WG01
Westerly granite #2	4	5	27	WG02
Westerly granite #4	4	10	53	WG04
monzonite #3	4	20	61	MONZ03
monzonite #4	4	35	62	MONZ04
monzonite #5	4	25	76	MONZ05
Carrara marble #1	5	20	39	M8_1
Carrara marble #2	5	25	44	M8_2
Fontainebleau sandstone #1	5	20	136	FBL01
Fontainebleau sandstone #2	5	10	43	FBL02
Fontainebleau sandstone #3	5	10	51	FBL03

168 **Table 1.** Experimental conditions of the eleven experiments. The number of scans is the total
 169 number of scans acquired throughout each complete experiment.

170 2.2. Data extraction

171 This analysis uses properties of the fracture networks identified in the X-ray tomograms.
 172 Following the experiment, we reconstruct the acquired radiographs into three-dimensional
 173 volumes that are 1600x1600x1600 voxels. One side length of a voxel is 6.5 μm . During
 174 reconstruction, we apply several corrections to remove noise, such as ring artefacts. We then
 175 remove remaining noise in the three-dimensional data using the image analysis software
 176 Avizo3D™, including the application of a non-local means filter (Buades et al., 2005). Using
 177 these three-dimensional volumes, we segment the solid rock from the pores and fractures. We
 178 use an algorithm similar to Otsu's thresholding technique to identify a global threshold between
 179 the solid material and the fractures and pores (McBeck et al., 2021). This thresholding technique
 180 is robust to noise (McBeck et al., 2021) and produces segmented scans with porosity similar to
 181 measured values (Renard et al., 2018).

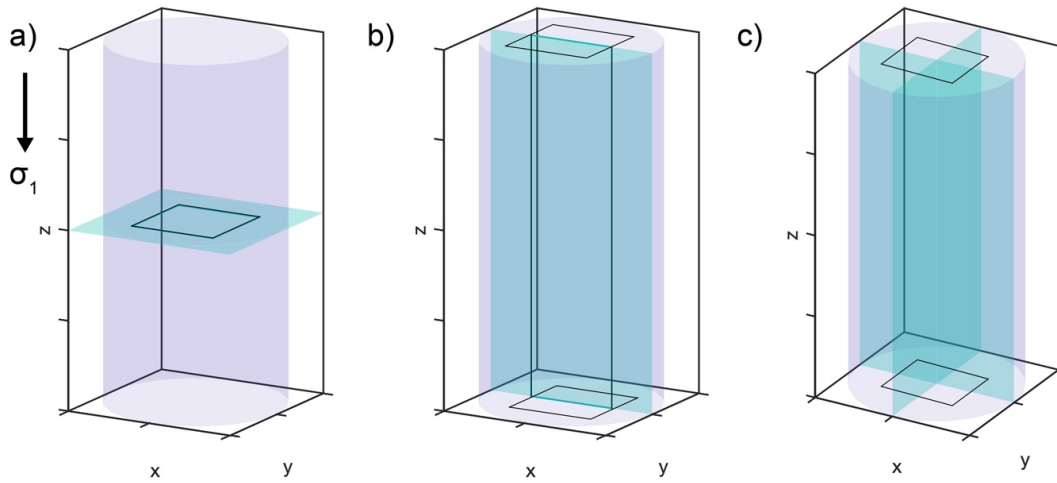
182 Because we aim to predict three-dimensional properties from two-dimensional
 183 measurements, we only consider a subset of the data so that the rounded edges of the rock
 184 cylinders do not influence the two-dimensional measurements. We only extract data within a
 185 rectangular prism at the center of the core, shown by the black rectangles in **Figure 3**. The size
 186 of the base of the prism depends on the width of the rock core. We set the positions of the sides
 187 of the base to $\frac{w}{2} - \frac{w}{4}$ to $\frac{w}{2} + \frac{w}{4}$, where w is the width of the core.

188 We test the influence of extracting the two-dimensional data along different orientations
 189 in order to constrain the best method of extracting cross sections of natural rock cores. We test
 190 four different methods of extracting two-dimensional slices: 1) acquiring horizontal slices along
 191 the vertical axis (z -axis and parallel to the maximum compression direction) (**Figure 3a**), 2)
 192 acquiring vertical slices along one of the horizontal axes (**Figure 3b**), 3) acquiring orthogonal
 193 vertical slices along both horizontal axes (**Figure 3c**), and 4) acquiring horizontal and vertical
 194 slices. Consequently, the area of the rock core captured in each method of slice extraction differs.
 195 We chose to compare slices of different areas in order to mirror the method of cutting natural
 196 rock cores.

197 We also test the influence of the amount of data provided to the models on the
 198 predictability of the three-dimensional properties. We vary the number of slices provided to the
 199 models from one to twenty slices, as well as all of the slices within the black rectangles shown in
 200 **Figure 3**. For the results of models trained on one slice, the methods of extraction that use
 201 multiple planes use one slice along each orientation, or two in total. When we take one slice, we
 202 use the slice within the center of the core, in either the horizontal or the vertical direction. When
 203 we take multiple slices, the slices are equally spaced throughout the rectangular prism (**Figure**
 204 **3**).

205 For each slice, and corresponding rectangular prism, at each differential stress step of
 206 each experiment, we calculate three properties. We focus on properties that control fluid flow
 207 within fracture networks: the porosity, the volume/area of the largest fracture, and the geometric
 208 tortuosity of the largest fracture. Note, we identify the largest fracture in the three-dimensional

209 data, and the largest fracture in each slice of the two-dimensional data separately. Consequently,
 210 the largest fracture identified in the two- and three-dimensional data at a given stress step of a
 211 given experiment may not be the same fracture. The geometric tortuosity is the ratio of the length
 212 of the true path between end points to the linear distance between end points (**Figure S2**). Here,
 213 we identify the end points of fractures as the locations of the fractures at the maximum and
 214 minimum z -coordinates. Thus, our tortuosity measurements reflect the path that a fluid must
 215 travel parallel to the maximum compression direction, and the long axis of the rock core.
 216 Because it is non-trivial to calculate tortuosity, we benefit from the Matlab function
 217 *bwdistgeodesic*, which calculates the distance of the true path between two points in two- and
 218 three-dimensions.



219

220 **Figure 3.** Sketch of the method of extracting the two-dimensional slices: horizontal slices within
 221 the x - y plane (a), vertical slices within the z - x plane (b), and orthogonal vertical slices, within the
 222 z - x plane and z - y plane (c). The z -axis is parallel to the maximum compression direction and
 223 vertical. We select the slices within a rectangular region (black) so that the cylindrical boundary
 224 of the rock core does not influence the calculated properties. When we take multiple slices, the
 225 slices are equally spaced throughout the core.

226 While the porosity considers all of the fractures in a particular slice or volume, the other
 227 two properties only consider the largest (most volumetric) fracture in the data. We focus on only
 228 the largest fracture for these properties, rather than all the fractures, because the volume and
 229 tortuosity of the largest fracture controls fluid flow. Following these calculations, we attain three
 230 datasets for each experiment corresponding to the three fracture network properties. Each of
 231 these datasets includes one three-dimensional measurement at each differential stress step of the
 232 experiment, and several hundred two-dimensional measurements: all of the horizontal slices
 233 along the vertical axis, and all of the vertical slices along both horizontal axes. Consequently, the
 234 data is arranged as a table where each row represents one differential stress step of a particular

235 experiment, and the columns include the three-dimensional measurement, and all of the two-
236 dimensional measurements.

237 2.3. Machine learning analysis

238 We design the machine learning models to predict three-dimensional properties from
239 two-dimensional measurements of the porosity, area of the largest fracture, and tortuosity of the
240 largest fracture. We test the influence of combining different rock types on the predictability of
241 the three-dimensional values. To combine data from multiple experiments, we append the data
242 sets described in the previous section. For example, one column in the data table contains the
243 two-dimensional value of the property at the horizontal slice at the position 600 voxels above the
244 base of the rock core throughout all of the scans acquired in all of the experiments included in
245 the data. Due to the different number of scans acquired in each experiment, the dataset of each
246 experiment contains different numbers of rows, or samples (**Figure S3**). To account for these
247 varying number of scans, and ensure that the properties of one experiment do not dominate the
248 other experiments, we extract the same numbers of samples of each experiment for the models
249 that include combinations of experiments. Thus, for the models that use data from all of the
250 experiments, we only take the number of samples from each experiment that match that lowest
251 number of samples (the granite #1 experiment) (**Table 1, Figure S3**). Because the fracture
252 networks grow with increasing loading, we select data from the end of the experiment.

253 We divide the data of the combined experiments into training and testing data sets such
254 that none of the data in the training set includes data in the testing set. We divide the data by
255 rows, so the training and testing datasets are unique in time (differential stress steps) for each
256 experiment. Because the performance of the models varies depending on how we split the
257 training and testing data sets, we report the performance of ten models that only differ in how the
258 training and testing data sets are randomly split. We use 30% of the data for testing, and 70% of
259 the data for training. Dividing the data by continuous blocks of time into training and testing
260 datasets does not produce lower model performance than dividing the data randomly by time.

261 We use both gradient boosting models (XGBoost) and linear regression models. We
262 chose XGBoost regression models because of its efficiency and accuracy (e.g., Friedman, 2001;
263 Bühlmann & Yu, 2003; Chen & Guestrin, 2016). We scale the features using the RobustScaler of
264 SciKit learn, which scales the data using the 25th and 75th quantile of the data (Pedregosa et al.,
265 2011). We perform a grid search over the hyperparameter-space to find the best set of
266 hyperparameters (Lundberg & Lee, 2017).

267 We also apply a simpler algorithm, linear regression, because of the interpretability of the
268 parameters of the trained models. Training linear regression models produces a set of coefficients
269 with one coefficient for each feature, or two-dimensional slice in this analysis, so that the three-
270 dimensional property is estimated as a linear combination of the features weighted by each
271 coefficient. From these coefficients, we aim to derive a function between the two- and three-
272 dimensional properties. For the models that predict the fracture volume and porosity, we force
273 the y -intercept of the regression model to intersect the origin because we suspect that two-
274 dimensional measurements of volume or porosity that are near zero should produce three-

275 dimensional values of zero. For these models, we do not scale the features so that the coefficients
 276 of the linear regression models are more interpretable.

277 We then develop gradient boosting models using the statistics of sets of two-dimensional
 278 observations. In particular, we subdivide each scan into sets of 20 vertical two-dimensional
 279 slices, and then calculate a range of statistics on the two-dimensional values measured in each
 280 slice, thereby producing a set of statistics for each group of 20 vertical slices of each scan. These
 281 statistics include: the mean, standard deviation, coefficient of variation, skewness, kurtosis,
 282 minimum, maximum, and the 10th, 25th, 50th, 75th, and 90th percentile of the dataset. Changing
 283 the number of slices within each group from 10 to 50 does not influence the key results. We only
 284 focus on the results of models developed with sets of vertical slices because our analyses indicate
 285 that the slice orientation does not systematically control the model performance, as described in
 286 the Results section. Similar to the other analyses, we vary the amount of data provided to the
 287 models from 10% to 90%. We randomly select ten different portions of the data with the given
 288 percentage and then develop ten different models with these varying parts of the data.

289 Because in this analysis we aim to determine which statistic of the two-dimensional
 290 observations provides the most useful information, we examine the impact of each feature (e.g.,
 291 statistic) on the predictions of the model using a widely used metric: Shapely Additive
 292 Explanations (SHAP) (e.g., Lundberg & Lee, 2017). We compare the mean absolute value of the
 293 SHAP (mean |SHAP|) of each feature across all of the samples, and so focus on the overall
 294 influence of that feature on the model prediction. Similar to the other machine learning analyses,
 295 we divide the data into training and testing datasets by time such that none of the scans that occur
 296 in the training dataset occur in the testing dataset. Because we develop ten different models for
 297 each model of varying amounts of data, we calculate a normalized importance of the mean
 298 |SHAP| value, s , as $s/\max(s)$ for each model, \hat{s} . We weight this normalized importance by the
 299 R^2 score of the model and then find the mean of these values across all the models, $s_w =$
 300 $\sum(R^2\hat{s})/n$, where n is the number of models, so that more accurate models (with higher R^2) will
 301 have a greater influence on the results than less accurate models. The distribution of s_w thus
 302 indicates the relative importance of each feature on the model predictions across several models.

303 **3 Results**

304 3.1. Predicting three-dimensional properties with gradient boosting models

305 First, we compare the performance of the gradient boosting models (XGBoost) developed
 306 for all of the experiments combined together. To assess model performance, we compare the R^2
 307 scores of the models, which represent the correlation coefficients between the observed and
 308 predicted three-dimensional values (**Figure 4**). High positive R^2 scores (0.8-1.0) indicate strong
 309 correlations between the observed and predicted values, while scores 0.4-0.7 indicate moderate
 310 correlations, and scores <0.4 indicate weak or non-existent correlations. To identify the best
 311 approach to rock core thin-section extraction and field analyses of fracture networks, we
 312 compare the influence of extracting slices from different orientations relative to the maximum
 313 compression direction, including horizontal and vertical slices, orthogonal vertical slices, and
 314 both horizontal and vertical slices (e.g., **Figure 3**). To assess the influence of the number of two-
 315 dimensional observations on the predictions, we also compare the performance of models
 316 developed with varying amounts of data, from one to twenty slices in increments of two slices,

317 and also all of the slices. **Figure 4** shows the mean \pm standard deviation of the R^2 scores of the
318 ten models developed for each fracture network property, and number and type of data, which
319 only differ in how the training and testing are split.

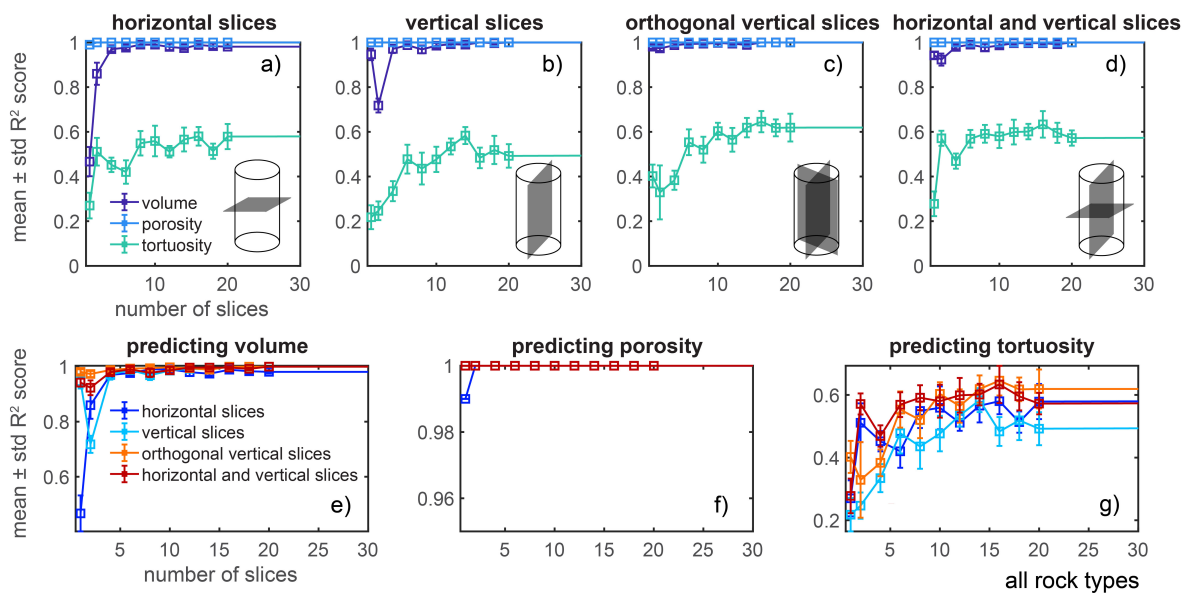
320 The models that predict the porosity and volume perform better than the models that
321 predict the tortuosity (**Figure 4a-d**). For example, the mean R^2 score of the models developed
322 with one horizontal and one vertical slice are: 1) 0.99 (porosity), 2) 0.94 (volume), and 3) 0.28
323 (tortuosity). Even when the models have access to all of the slices, they can only predict the
324 tortuosity with a mean R^2 score of 0.68, compared to the R^2 scores near 1.0 for the other
325 properties (**Figure 4, Figure 5**). This trend holds regardless of the orientation of the extracted
326 slices. This result suggests that it may be more difficult to derive a function between the two- and
327 three-dimensional tortuosity compared to the other properties.

328 Increasing the amount of data generally increases the performance of the models, as
329 expected (**Figure 4, Figure 5**). However, the models that predict the porosity using all of the
330 rock types perform exceptionally well using only one slice (**Figure 4**). Similarly, the models that
331 predict the volume of the largest fracture perform very well using only about four slices,
332 regardless of the method of slice extraction. Consequently, the difference in the model
333 performance when using 20 slices or one slice (porosity) to four slices (volume) is minor (<0.005
334 of the R^2 score). The influence of the amount of data on the model performance is most
335 significant for the property that the models struggle to predict: the tortuosity. Thus, extracting
336 many two-dimensional slices of a system is most beneficial when estimating the tortuosity and
337 related properties, such as the permeability. In contrast, when estimating the porosity or volume
338 of the largest fracture, only one to four two-dimensional measurements may be required for
339 reasonably accurate estimates.

340 In contrast to expectations, the different methods of slice extraction produce models that
341 perform similarly to each other when they use more than one slice of the data (**Figure 4, Figure**
342 **5a-c**). We expected that vertical slices (parallel to the maximum compression direction) may
343 produce more accurate models than horizontal slices because they sample a larger area, and
344 therefore produce stronger positive correlations between the two- and three-dimensional
345 properties (**Text S1, Figure S4, Figure S5, Figure S6**). In agreement with these expectations,
346 when the models use one slice, horizontal slices produce less successful models than vertical
347 slices for the models that predict the porosity and volume. Both the horizontal and vertical slices
348 produce poorly performing models with 0.2-0.3 R^2 scores when the models predict the tortuosity
349 (**Figure 5c**). We expected that models developed with two orthogonal vertical slices or both
350 vertical and horizontal slices may perform better than models developed with only horizontal or
351 vertical slices because they sample more area, and at perpendicular orientations. In contrast to
352 this idea, the models that use orthogonal vertical slices or both horizontal and vertical slices do
353 not perform significantly better than the other models. The comparable performance of the
354 models developed with more than one slice at perpendicular orientations to each other and series
355 of parallel slices indicates that it may not be critical to obtain field observations and thin-sections
356 of rock cores at perpendicular orientations in order to make robust estimates of the fracture

357 network geometry, and thus fluid flow. Instead, several parallel observations may be sufficient
 358 for accurate estimates.

359 Next, we compare the performance of models developed with all of the rock types to
 360 models developed for individual rock types. We expect that models developed for specific rock
 361 types may perform better than models developed for all of the experiments because different
 362 relationships may exist between the two- and three-dimensional data in different rock types. For
 363 example, the equation that relates the two-dimensional porosity to the three-dimensional porosity
 364 may differ between the sandstone and granite because sandstone hosts many quasi-spherical
 365 pores, whereas the granite contains fractures and pores with shapes closer to cigars, rather than
 366 spheres (e.g., Renard et al., 2018). We focus on the models developed using both horizontal and
 367 vertical slices here (**Figure 5d-f**).

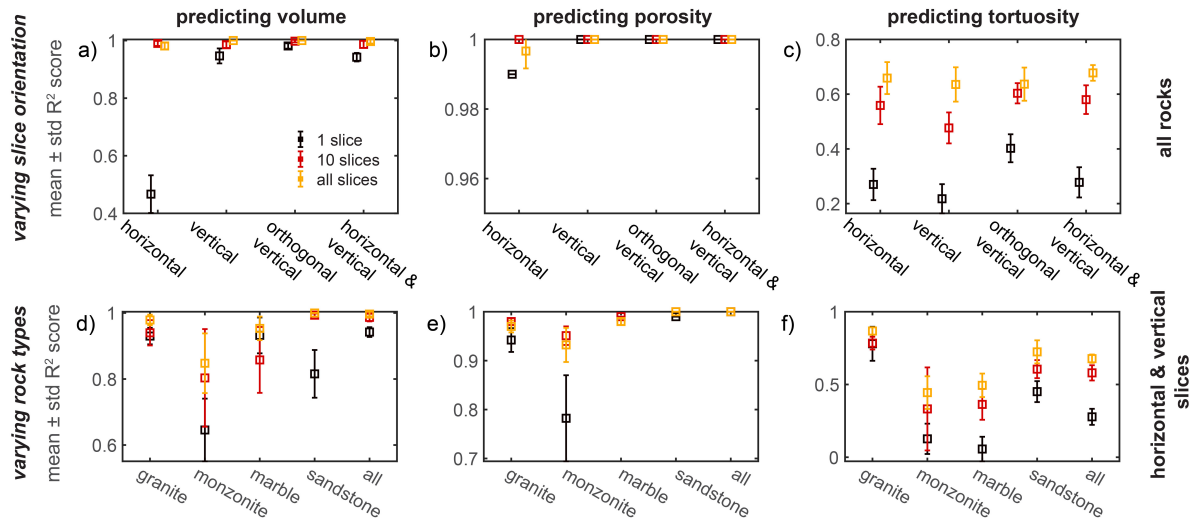


368

369 **Figure 4.** Performance of the gradient boosting models developed for all of the rock types using
 370 horizontal slices (a), vertical slices (b), orthogonal vertical slices (c), and both horizontal and
 371 vertical slices (d) to predict the volume (e), porosity (f) and tortuosity (g). For the models
 372 developed with the orthogonal vertical slices, and the horizontal and vertical slices, the score
 373 reported for one slice indicates the score of models developed with either one slice along both
 374 orthogonal horizontal axes, or one slice along the vertical axis and a horizontal axis. The models
 375 struggle to predict the tortuosity, but predict the volume and porosity with strong correlations
 376 between the predicted and observed values. The orientation of the extracted slices does not
 377 systematically influence the model performance.

378 Consistent with the trend of the correlation coefficients (**Text S1, Figure S6**), the models
 379 developed for all of the rock types do not perform worse than the models developed for the
 380 individual rock types (**Figure 5**). Instead, some of the models developed for individual rock
 381 types perform worse than the models developed with all of the data (**Figure 5d, e**). The models
 382 that predict the tortuosity differ somewhat from this trend. The performance of the models that
 383 predict the tortuosity using one slice of the data of all the rock types perform worse than models
 384 developed with only the granite data, and models developed with only the sandstone data.

385 However, the models developed with all of the rock types perform better than models developed
 386 with only the monzonite data, and models developed with only the marble data. Consequently,
 387 the models developed using all of the rock types perform similarly successfully as the models
 388 developed for the individual rock types when they predict the volume and porosity, and perform
 389 better than half of the rock types when they predict the tortuosity. This result contradicts the
 390 expectation that different relationships link the two- and three-dimensional properties in different
 391 rock types, such as sandstone and granite.



392
 393 **Figure 5.** Performance of the gradient boosting models developed for all of the rock types using
 394 the four methods of slice extraction (a-c), and each individual rock type and all of the rock types
 395 using both horizontal and vertical slices (d-f). The performance of models developed with one
 396 slice (black), 10 slices (red), or all of the slices (yellow) are shown with different colors. The
 397 model performance does not systematically depend on the method of slice extraction (a-c). The
 398 models developed using all of the rock types perform better than models developed for
 399 individual rock types (d-f).

400 3.2. Deriving a relationship between two-dimensional and three-dimensional properties

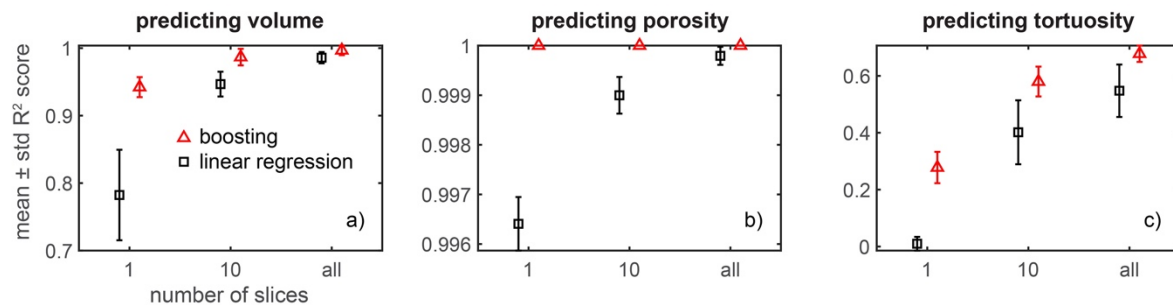
401 The strong performance of the gradient boosting models suggest that a less complex
 402 algorithm may be able to predict the three-dimensional properties from the two-dimensional
 403 observations with success. Here, we use linear regression models to predict the three-
 404 dimensional properties because these models enable identifying a function between the two-
 405 dimensional measurements and the three-dimensional properties. In particular, a trained linear
 406 regression model includes a suite of coefficients, one for each slice in this analysis, c_i , that
 407 provides an equation between the two-dimensional measurements (i.e., features), f_i^{2D} , and the
 408 three-dimensional property, p^{3D} , (Pedregosa et al., 2011):

409
$$p^{3D} = \sum_{i=1}^n c_i f_i^{2D} \quad \text{Eq. 1}$$

410 where n is the number of features: the number of two-dimensional slices in this analysis.
 411 Consequently, the three-dimensional property is estimated as a linear combination of the two-
 412 dimensional property measured at each slice multiplied by the associated coefficient, c_i . Due to

413 the simplicity of these types of models, we expect that the performance of the models will be
 414 worse than the performance of the gradient boosting models.

415 Indeed, the linear regression models perform with lower R^2 scores than the boosting
 416 models (**Figure 6**). However, the linear regression models perform reasonably well when they
 417 predict the volume and porosity using only one slice along both the vertical and horizontal axes,
 418 with moderate-strong correlations between the observed and predicted values (**Figure 6a-b**).
 419 Similar to the boosting models, the linear regression models do not predict the tortuosity with
 420 strong correlations between the predicted and observed values (**Figure 6c**). The linear regression
 421 models that use data from all of the experiments perform better than the models that use data
 422 from individual rock types (**Figure S7**), similar to the boosting models. This result lends further
 423 support to the idea that the relationships between two- and three-dimensional fracture network
 424 properties may be similar in porous granular rocks (sandstone) and lower porosity crystalline
 425 rocks (granite).



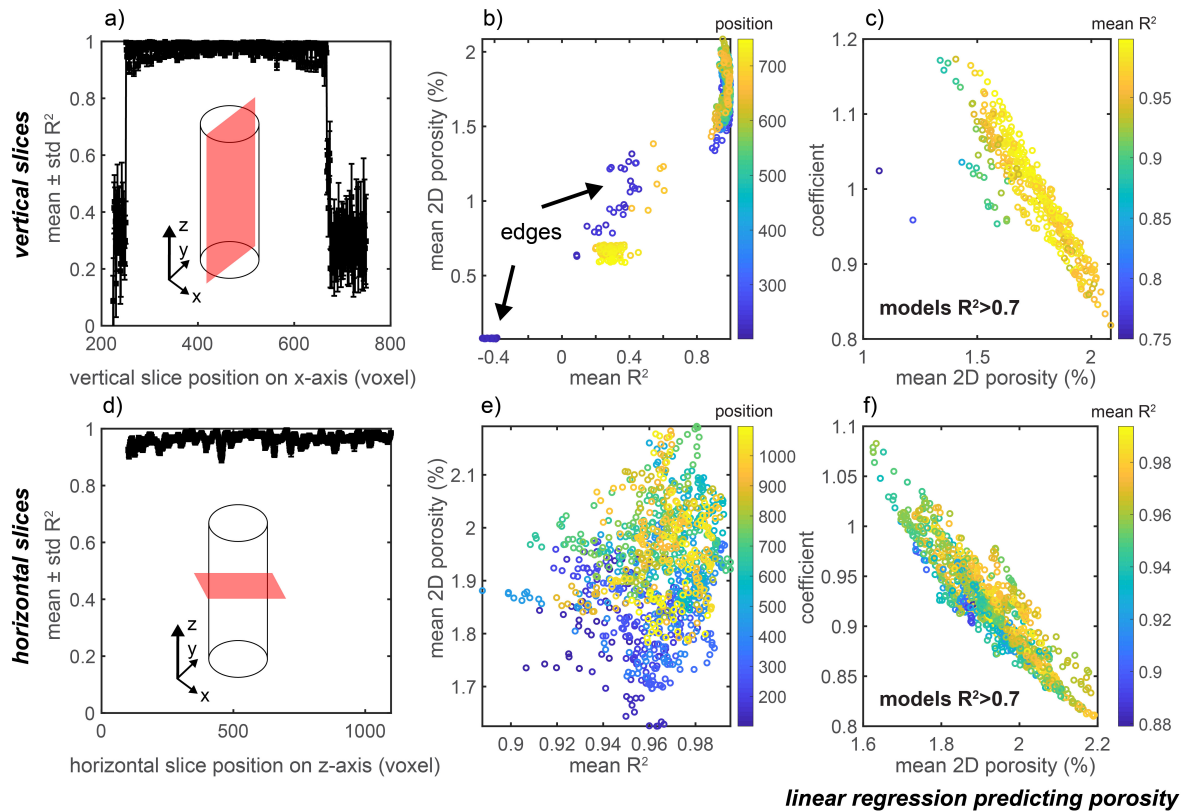
426

427 **Figure 6.** Performance of the gradient boosting models and linear regression models when
 428 predicting the volume (a), porosity (b), and tortuosity (c) using one, ten, and all of the slices,
 429 for data from all of the rock types, using slices along the horizontal and vertical axes. The boosting
 430 models perform better than the linear regression models. The linear regression models predict the
 431 volume of the largest fracture and porosity with strong correlations between the predicted and
 432 observed values.

433 The strong performance of the linear regression models that predict the porosity and
 434 volume suggest that we may examine their coefficients in order to constrain the equations that
 435 relate the two- and three-dimensional porosity and fracture volume. We expect that these two-
 436 and three-dimensional properties will be positively correlated to each other: higher two-
 437 dimensional porosity or fracture volume should indicate higher three-dimensional porosity or
 438 fracture volume.

439 To examine how the coefficients of the models relate to the two-dimensional properties,
 440 we focus on the results of the linear regression models that use one slice of the data, in either the
 441 vertical or horizontal direction, with data from all the experiments (**Figure 7**, **Figure 8**). As
 442 described in the Methods section, the models that use one vertical slice from one experiment
 443 sample one slice position in the rock core across all of the differential stress steps, and when the
 444 models use data from several experiments, they sample one position in all of the rock cores and
 445 all the associated stress steps. Because we expect that the value of the two-dimensional property
 446 will influence the magnitude of the coefficient, we compare the coefficient and mean of the two-

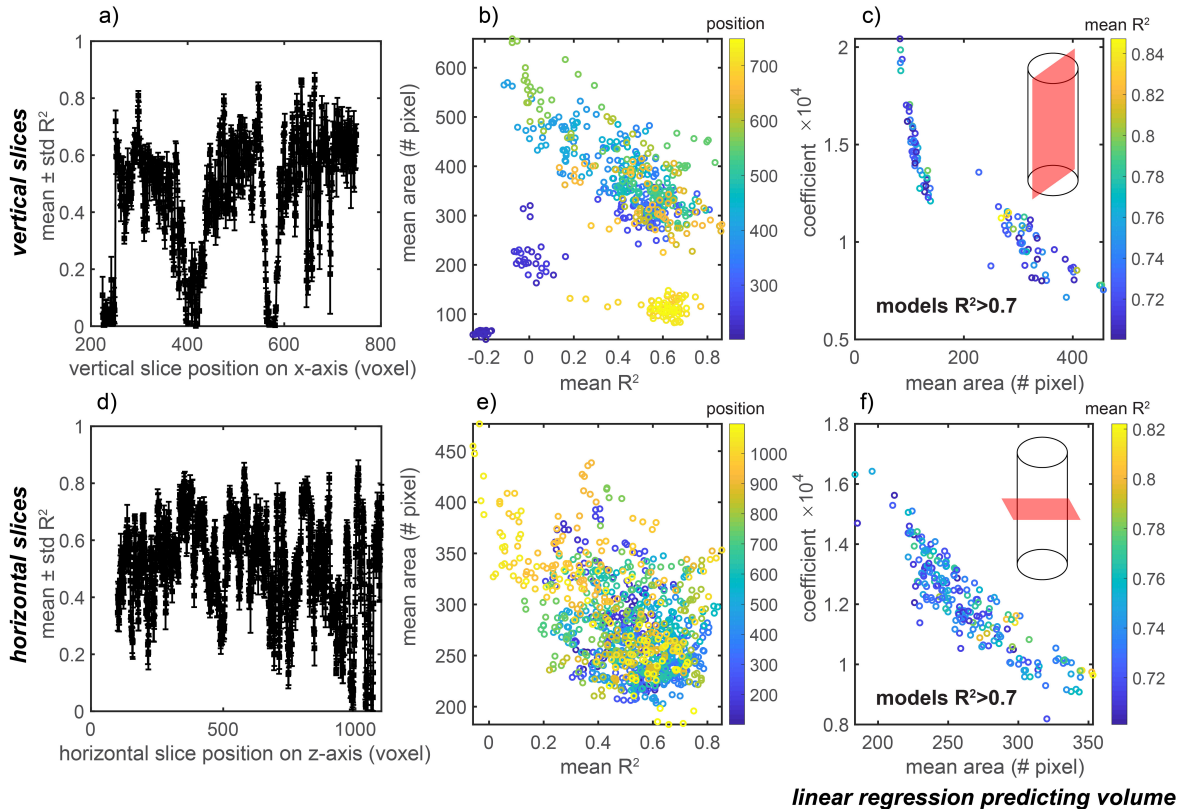
447 dimensional value across all of the slices at one particular location, and throughout all the
 448 differential stress steps and experiments.



449 **Figure 7.** Relationships between the model performance, two-dimensional porosity and
 450 coefficient of the linear regression models developed with data from all the experiments, with
 451 vertical (a-c) and horizontal (d-f) slices. a, d) Mean \pm one standard deviation of the R^2 of models
 452 developed from vertical slices (a) and horizontal slices (d) relative to their position along the x-
 453 or z-axis. These models only differ in how the training and testing data are split. b, e) The mean
 454 R^2 score of the models, and the corresponding mean two-dimensional porosity at the slice
 455 position used to develop the model. The color of the symbol indicates the position along the x- or
 456 z-axis of the model and two-dimensional measurement. The arrows in (b) highlight regions of the
 457 core at the edges that produce models with lower R^2 scores. c, f) The mean two-dimensional
 458 porosity and mean coefficient of the corresponding set of models for models with higher R^2
 459 scores (>0.7). The color of the symbol indicates the R^2 score of the model.

460 The position of the vertical slice within the cores influences the ability of the models to
 461 predict the porosity (**Figure 7a**). When the models use data at the edges of the cores, the R^2
 462 scores range from -0.4 to 0.5. However, when they use data within the central portion of the
 463 cores, the R^2 scores are >0.9 . The lower porosity at the edges of the cores may explain the lower
 464 model performance (**Figure 7b**). Our method of accumulating the data from the different
 465 experiments produces these apparent regions of lower porosity. Because the marble and
 466 sandstone cores are wider than the granite and monzonite cores, the database that includes data
 467 from all of the experiments have columns in which no porosity is reported for the thinner cores,

468 and in which non-zero porosity is reported for the wider cores. Thus, the models developed for
 469 these portions of the cores will likely be prone to low performance. However, this edge effect
 470 does not emerge when the models predict the volume of the largest fracture (**Figure 8a**). When
 471 the models predict the largest fracture, the position of the vertical slices that produce the most
 472 incorrect models include the edge of the cores, as well as positions within the center of the cores,
 473 near 400 and 600 voxels from the edge of the cores (**Figure 8a**). In contrast to the strong
 474 influence of position on the model performance when they predict the porosity using vertical
 475 slices, the position of the horizontal slices does not lead to systematic changes in the R^2 scores,
 476 for both the models that predict the porosity (**Figure 7d**) and volume (**Figure 8d**).



477

478 **Figure 8.** Relationships between the model performance, two-dimensional volume and
 479 coefficient of the linear regression models developed with data from all the experiments, with
 480 vertical (a-c) and horizontal (d-f) slices. The format of the figure is the same as **Figure 7**.

481 Because the values of the coefficients c_i (Eq. 1) derived from the linear regression
 482 models may depend on the magnitude of the fracture network property at a particular slice, we
 483 now compare the coefficient and mean of the two-dimensional values across all of the slices at
 484 one particular location, and throughout all the differential stress steps and experiments. For the
 485 models that predict the porosity with R^2 scores greater than 0.7, the coefficients range from about
 486 0.8 to 1.1 (**Figure 7c, f**). The ranges of the 25th-75th percentile of the coefficients for the models
 487 developed with horizontal slices and vertical slices are 0.89-0.95 and 0.95-1.05, respectively
 488 (**Figure S8**). For the models that predict the volume of the largest fracture, the coefficients range
 489 from about 0.8-2.0 $\cdot 10^4$ (voxels/pixels) (**Figure 8c, f**). The units of these coefficients are the

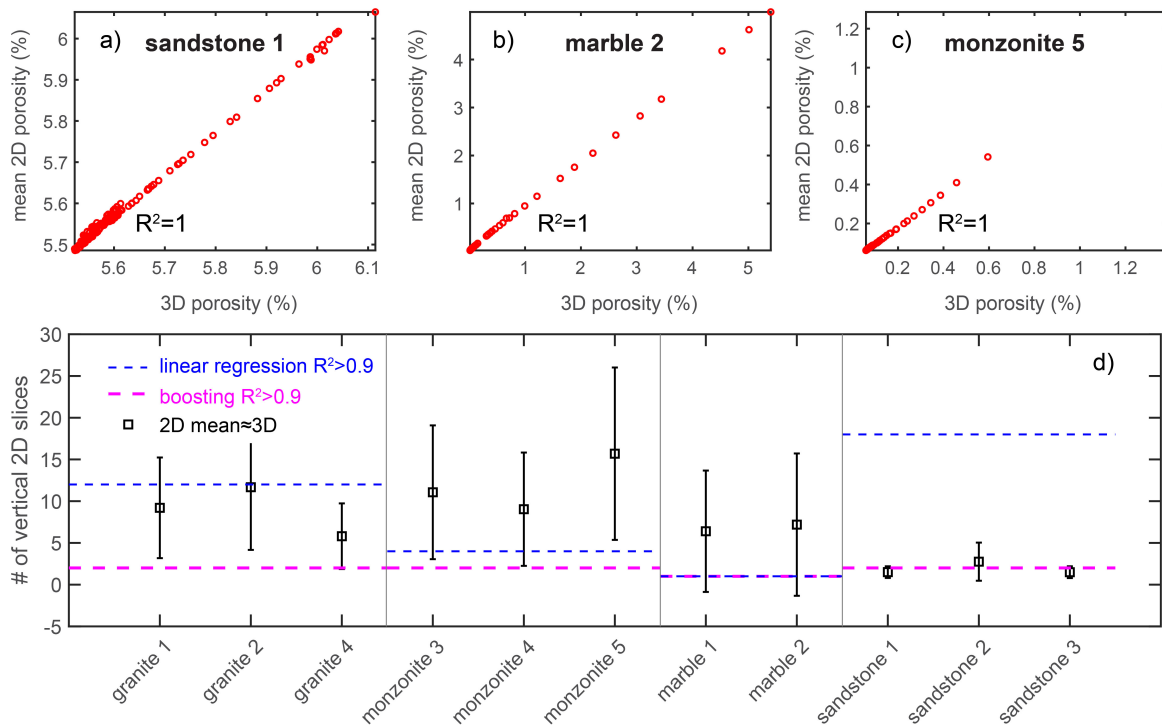
490 number of voxels/pixels because they use the fracture area (pixels) to estimate the fracture
 491 volume (voxels) with the equation: fracture volume (voxels)= c (voxels/pixels)·fracture area
 492 (pixels), where c is the coefficient. The ranges of the 25th-75th percentile of the coefficients for
 493 the models developed with horizontal slices and vertical slices to predict the fracture volume are
 494 $11 \cdot 10^3$ to $13 \cdot 10^3$ (voxels/pixels) and $9 \cdot 10^3$ to $14 \cdot 10^3$ (voxels/pixels), respectively (**Figure S8**).
 495 These ranges are consistent with our expectation that a positive correlation exists between the
 496 two- and three-dimensional porosity and fracture volume. The precise values of the coefficients
 497 for the models that predict the porosity suggest that horizontal slices of rock cores may tend to
 498 overestimate the three-dimensional porosity as they require coefficients less than one, with mean
 499 values of 0.92 for the models with R^2 scores greater than 0.7. In contrast, vertical slices can
 500 provide a close approximation of the three-dimensional porosity, requiring coefficients close to
 501 one, with mean values of precisely 1.00.

502 There is a negative correlation between the two-dimensional porosity and the model
 503 coefficient, for both the vertical (**Figure 7c**) and horizontal slices (**Figure 7f**). Thus, higher two-
 504 dimensional porosity leads to lower coefficients for the models that predict the porosity. Similar
 505 to these models, the models that predict the volume also host a negative correlation between the
 506 two-dimensional property and the coefficient (**Figure 8c, f**). This negative correlation arises
 507 because slices that produce anomalously higher values of porosity and fracture area require a
 508 lower coefficient to approximate the three-dimensional value than slices that produce lower
 509 values.

510 3.3. Comparing machine learning algorithms to simple statistics

511 Examining the relationship between the three-dimensional porosity, and the two-
 512 dimensional measurements (e.g., **Figure S4-S6**) suggest that calculating simple statistics of the
 513 population of two-dimensional slices may closely approximate the three-dimensional porosity. In
 514 particular, the correlation between the mean of the vertical two-dimensional slices at each
 515 differential stress step and the three-dimensional porosity of a given step is strong, with
 516 correlation coefficients near one (e.g., **Figure 9a-c**). Due to the ability of this simple statistic to
 517 approximate the three-dimensional porosity, we identify when the machine learning models
 518 predict the three-dimensional porosity with greater success than calculating the mean, given the
 519 same amount of data. In particular, we find the number of vertical slices for which the mean of
 520 these slices is within 5% of the three-dimensional value at each stress step of each experiment,
 521 n_m (e.g., **Figure S9, Figure 9**). We randomly select a given number of slices throughout the rock,
 522 calculate the mean of those slices, and then determine if the two-dimensional mean falls within
 523 5% of the three-dimensional value. If the two-dimensional mean does not match the three-
 524 dimensional value, then we increase the number of slices and repeat the process. To account for
 525 heterogeneity in the rock sample, we repeat this selection process 10,000 times, thereby sampling
 526 a different population of slices. We then compare the mean \pm one standard deviation of n_m
 527 throughout each experiment to the number of vertical slices required for the machine learning
 528 algorithms to produce R^2 scores >0.9 , n_a (**Figure 9d**). In order to compare these values, we use

529 the models developed for the individual rock types with the vertical slices, for both the gradient
 530 boosting models and the linear regression models.



531

532 **Figure 9.** Comparing the performance of a simple statistic (the mean) to the machine learning
 533 algorithms. a-c) Relationship between the three-dimensional porosity and the mean two-
 534 dimensional porosity calculated from the vertical slices in three example experiments: a)
 535 sandstone #1, b) marble #2, and c) monzonite #5. The correlation coefficients between these
 536 values are 1.0 in each of these experiments. d) Comparing the number of vertical slices for which
 537 the mean of the slices is within 5% of the three-dimensional mean at each stress step (scan) of
 538 each experiment, and the number of slices required by both machine learning algorithms to
 539 predict the porosity with R^2 scores greater than 0.9. The blue and pink dashed lines indicate the
 540 linear regression and boosting results, respectively. Calculating the mean provides similarly
 541 accurate estimates as the gradient boosting models for the most homogeneous rock types
 542 (sandstone), given the same amount of data. For the more heterogeneous rocks, the machine
 543 learning algorithms provide more accurate predictions of the three-dimensional porosity than
 544 calculating the mean.

545 The heterogeneity of the rock determines if calculating the mean requires less data than
 546 the machine learning models in order to make successful predictions. For the boosting models,
 547 the n_a is generally smaller than the n_m , except for the sandstone experiments, indicating the
 548 superiority of the machine learning algorithms for all the experiments except the sandstone
 549 experiments (**Figure 9d**). The sandstone cores require a similar n_m and n_a . For the linear
 550 regression models, n_m is lower than n_a for two rock types: the granite and sandstone, indicating
 551 the superiority of calculating the mean rather than using linear regression for these rocks. The
 552 lower average and standard deviation of the n_m of the sandstone cores indicates that the
 553 sandstone develops the most homogeneous pore and fracture networks of the rocks examined

554 here. These homogeneous networks then enable simple statistics to provide more accurate
555 estimates of the three-dimensional property than the linear regression models for the same
556 amount of data. For the more heterogeneous rocks, although they host strong correlations
557 between the three-dimensional porosity and mean two-dimensional porosity calculated with all
558 of the vertical slices (**Figure 9a-c**), the machine learning algorithms require less information to
559 successfully predict the three-dimensional property than the mean (**Figure 9d**). This analysis
560 thus reveals the rock types for which simple statistical approaches may provide reasonably
561 accurate estimates of the three-dimensional porosity.

562 3.4. Identifying the statistics that predict the three-dimensional properties

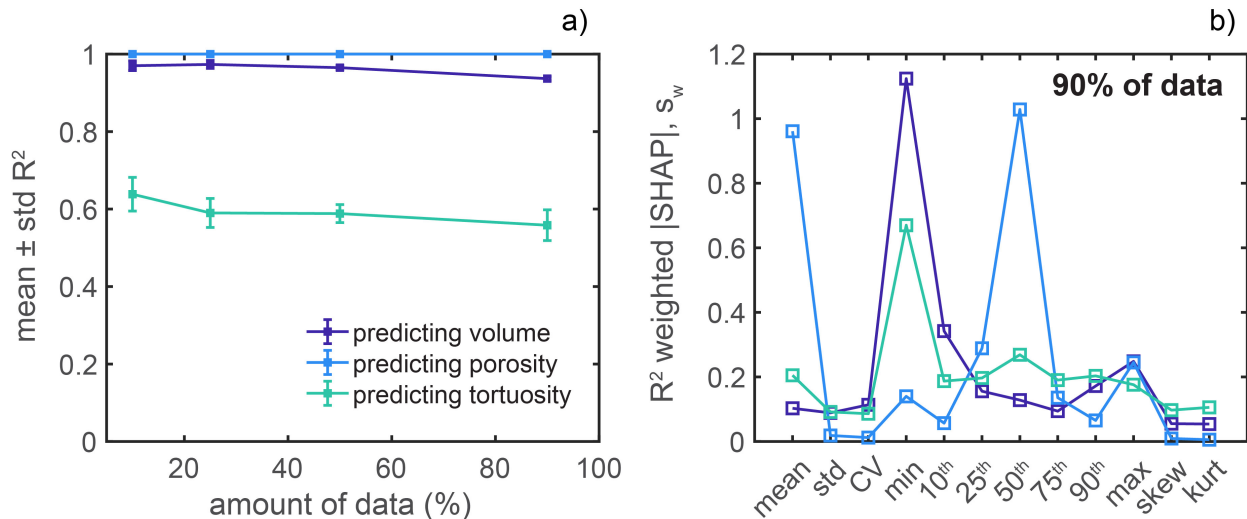
563 The analysis of the previous section indicates that statistical approaches can help build
564 equations between the two- and three-dimensional porosity at least in homogeneous rocks, such
565 as sandstone. However, we cannot apply this approach to determine the usefulness of statistics
566 for the other two properties: the volume and tortuosity of the largest fracture. Instead, we may
567 use machine learning to identify the statistics that are most beneficial to predictions of the three-
568 dimensional volume and tortuosity. To identify these statistics, we reformat our dataset of two-
569 dimensional observations so that the models use the statistics of several two-dimensional
570 observations to predict the three-dimensional value. We focus on the results of models developed
571 using all of the rock types and vertical slices because our previous analyses indicate that
572 combining several rock types can produce more accurate models, and that the orientation of the
573 observation does not systematically control the model performance (**Figure 5**).

574 Comparing the performance of models developed from statistics of the two-dimensional
575 observations indicates that the models predict the porosity and volume of the largest fracture
576 with success, but struggle to predict the tortuosity (**Figure 10a**), similar to the models developed
577 from the raw slices. In particular, the mean R^2 scores for models developed with varying
578 amounts of data are 0.99 (porosity), 0.96 (volume) and 0.59 (tortuosity). An additional similarity
579 is that the amount of data provided to the models does not lead to a continuous improvement of
580 the model performance. In particular, varying the amount of data provided to the models
581 developed using statistics from 10% to 90% of the available data does not change the R^2 score by
582 more than 0.03 for the models that predict the porosity and volume of the largest fracture. For the
583 models that predict the tortuosity, the mean R^2 score in fact decreases by about 0.08 when the
584 amount of data increase from 10 to 90%, in contrast to the idea that more data invariably leads to
585 better model performance. Because we randomly select the data provided to the models, the
586 decrease in model performance does not arise from selecting data earlier or later in loading, for
587 example.

588 To identify the statistics that are most useful to the predictions, we focus on the models
589 developed with 90% of the data. Comparing the features that produce the highest R^2 -weighted
590 |SHAP| value, s_w , for each set of models indicates that the models that predict the porosity
591 primarily depend on the mean and 50th percentile (**Figure 10b**). The dependence of the porosity
592 models on these statistics agrees with the ability of the mean of the two-dimensional porosity to
593 estimate the three-dimensional porosity using less slices than the machine learning models for
594 the sandstone experiments (**Figure 9**). Moreover, the dependence of the porosity models on these
595 statistics suggests that when the data from multiple rock types are combined together, the

596 average and median of the two-dimensional porosity measurements may provide better estimates
 597 of the three-dimensional porosity than the other tested statistics.

598 In contrast to the models that predict the porosity, the models that predict the other two
 599 properties do not strongly depend on the mean (**Figure 10b**). Surprisingly, the models that
 600 predict the volume and tortuosity of the largest fracture depend primarily on the minimum area,
 601 or minimum tortuosity, of the largest fracture identified in the group of two-dimensional slices.
 602 This result suggest that the extreme values of the population of the largest fracture identified in a
 603 particular two-dimensional slice (the minimum value) provides the most useful information
 604 about the properties of the largest fracture identified in the full three-dimensional scan.



605 **Figure 10.** Score (a) and R^2 weighted |SHAP| value distribution (b) of models developed using
 606 the statistics of groups of vertical two-dimensional measurements for all of the rock types
 607 combined: the results for models with all of the tested amounts of data (a), and the results for
 608 only the models with 90% of the data (b). The statistics used as features are the mean, standard
 609 deviation (std), coefficient of variation (CV), minimum, 10th-90th percentile, maximum,
 610 skewness (skew), and kurtosis (kurt). a) The models that predict the volume and porosity
 611 perform very well, and better than the models that predict the tortuosity. Varying the amount of
 612 data from 10-90% does not lead to large changes in the mean R^2 score. b) The models that
 613 predict the porosity primarily depend on the mean and median value. In contrast, the models that
 614 predict the properties of the largest fracture primarily depend on the minimum value in a group
 615 of two-dimensional observations.
 616

617 4 Discussion

618 4.1. Predictability of three-dimensional properties of fracture networks

619 The present study enables a direct comparison of the predictability of several fracture
 620 network characteristics that control fluid flow, and thus the potential ability to derive an equation
 621 between the two- and three-dimensional measurements. The results indicate that it may be more
 622 difficult to derive a function between the two- and three-dimensional tortuosity than the other
 623 properties (**Figure 4**). This difficulty of predicting the three-dimensional tortuosity is consistent
 624 with previous work that found that using two-dimensional estimates of fluid flow leads to

625 erroneous estimates of the three-dimensional flow properties, such as the permeability (e.g., Li et
626 al., 2005; Duda et al., 2011; Mostaghimi et al., 2013; Lang et al., 2014; Marafini et al., 2020).
627 This result is also consistent with work that compared the size of the representative elementary
628 volume (REV) for permeability, porosity, and specific surface area (Mostaghimi et al., 2013).
629 The REV is the minimum volume for which the property of interest (i.e., permeability) varies
630 less than some threshold from the property calculated in larger volumes (e.g., Bear, 1988; Zhang
631 et al., 2000). Mostaghimi et al. (2013) found that the REV for the permeability was up to twice
632 as large as the REV for the porosity and specific surface area in granular rocks, including
633 carbonate and sandstone. The larger REV suggests that the permeability distribution was more
634 heterogeneous than the porosity and the specific surface area. Because the permeability depends
635 on the tortuosity of the fracture network, the larger REV of the permeability relative to the
636 porosity (Mostaghimi et al., 2013) agrees with the excellent performance of the machine learning
637 models in the present analysis when they predict the porosity and volume of the largest fracture,
638 and mediocre performance of the models when they predict the tortuosity (**Figure 4**). The more
639 heterogeneous and anisotropic distribution of the tortuosity of the fracture network compared to
640 the other properties, and the importance of considering connectivity in three-dimensions,
641 produce both results.

642 Tortuosity, and therefore permeability, are thus more difficult to predict in the laboratory
643 than other properties of the fracture network. Similarly, estimates of the subsurface permeability
644 can depend on the scale of the measurement. In particular, estimates of permeability derived
645 from core samples tend to be lower than the estimates of permeability derived from pumping
646 tests (e.g., Rovey & Cherkauer, 1995; Sánchez-Villa et al., 1996; Raghavan, 2006). These
647 studies suggest that permeability increases with spatial scale. The presence of stratification,
648 layering and other heterogeneities with a spatial dimension larger than the typical core sample
649 produces this spatial dependence (e.g., Raghavan, 2006). Laboratory data further supports the
650 idea that permeability increases with spatial scale (e.g., Schulze-Makuch et al., 1999). However,
651 simulations indicate that permeability can both increase and decrease with spatial scale (e.g.,
652 Sahimi et al., 1986; Nordahl & Ringrose, 2008; Esmailpour et al., 2021; Ghanbarian, 2022).
653 Consequently, this previous work demonstrates that varying the spatial scale in three-dimensions
654 can change estimates of permeability, and the present analysis demonstrates that it is similarly
655 difficult to estimate the three-dimensional tortuosity (and thus permeability) from two-
656 dimensional observations. The dimensional contraction from three to two dimensions thus
657 produces a similar effect as varying the spatial length scale in three dimensions.

658 The greater predictability of the porosity suggests that we may be able to estimate the
659 three-dimensional mechanical properties of rocks that depend on the porosity (i.e., Young's
660 modulus) with more success than the properties that depend on the tortuosity (i.e., permeability).
661 Consequently, estimates of the permeability may require direct numerical computation of the
662 flow within the three-dimensional system, such as solving for Stokes flow or performing lattice
663 Boltzmann simulations (e.g., Bultreys et al., 2016). Moreover, the relationship between the two-
664 and three-dimensional estimates of elastic moduli may be easier to constrain than the
665 corresponding relationship for the permeability. Indeed, recent work has successfully estimated
666 three-dimensional elastic moduli using the aspect ratio of the pores reconstructed from three
667 orthogonal two-dimensional slices of Berea sandstone and Grosmont carbonate (Karimpouli et
668 al., 2018). In summary, because two-dimensional measurements of porosity can be closely linked

669 to the three-dimensional porosity, properties that depend on the porosity, such as the elastic
670 moduli, may be similarly predictable.

671 4.2. Amount and type of data required for successful predictions

672 The analysis helps constrain the amount and type of data required for successful
673 estimates of the three-dimensional properties. One may expect that increasing the amount of data
674 provided to the models would increase the model performance. Our results agree with this
675 expectation: higher numbers of two-dimensional estimates generally produce larger R^2 scores
676 (**Figure 4, Figure 5, Figure 6**). However, the performance of the models does not continually
677 increase with the number of two-dimensional slices (**Figure 4**). Instead, the model performance
678 increases relatively rapidly over at most ten slices, and then does not change significantly
679 between ten slices, and all of the available slices (e.g., **Figure 5**). Only one to four slice positions
680 are required for reasonably accurate estimates of the porosity and volume of the largest fracture.

681 This analysis enables direct comparison of the usefulness of examining two-dimensional
682 slices that are oriented parallel (vertical) or perpendicular (horizontal) to the maximum
683 compression direction, as well as combinations of these orientations. One may expect that the
684 models developed with both horizontal and vertical slices would provide the most accurate
685 estimates. However, the results do not indicate that one method systematically produces higher
686 model performance (**Figure 4, Figure 5a-c**). This result suggests that the orientation of thin-
687 sections or field measurements may not exert a significant control on estimates of the three-
688 dimensional property. Moreover, several parallel two-dimensional observations may provide
689 comparable estimates of the three-dimensional system as several perpendicular two-dimensional
690 observations. The orientation of the measurement could be more significant for properties in
691 rocks that are more anisotropic than those analyzed here, such as layered sedimentary rock.

692 This analysis provides further insight into the influence of rock type on the predictability
693 of the fracture network characteristics. One may expect that different relationships can develop
694 between the two- and three-dimensional data in different rock types. For example, the equation
695 that relates the two-dimensional porosity to the three-dimensional porosity may differ between
696 the sandstone and crystalline rocks because sandstone hosts many quasi-spherical pores (e.g.,
697 Dong & Blunt, 2009), whereas the granite contains fractures and pores with more anisotropic
698 shapes (e.g., Renard et al., 2018). If such different relationships exist, one would expect that the
699 performance of the models developed for individual rock types would be higher than the models
700 developed for a combination of rock types. In contrast, the results indicate that the models
701 developed using all of the experimental data perform better than or similarly to the models
702 developed using individual rock types (**Figure 5d-f**). This trend may arise in part from the larger
703 amount of data provided to the models developed for all the rock types compared to the models
704 developed for individual rock types. However, the higher values of the correlation coefficients
705 for the data accumulated from all of the experiments compared to the data from individual
706 experiments (**Figure S6**) suggest that the content of the data also influences the model
707 performance, and not only the amount of data. Previous analyses that link two- and three-
708 dimensional properties have tended to focus on specific rock types (e.g., Karimpouli et al.,
709 2018), rather than accumulating data from both low porosity crystalline rocks and granular rocks.
710 Moreover, previous analyses have identified specific failure criteria that are applicable to porous
711 granular rock, such as sandstone, but not to low porosity crystalline rock with interlocking

712 minerals (e.g., Wilshaw, 1971; Zhang et al., 1990). Similarly, theories from linear fracture
713 mechanics that relate the geometric properties of individual fractures, including the length and
714 orientation, to their propensity for propagation using the stress intensity factor do not explicitly
715 account for the presence of nearby quasi-spherical pores (e.g., Paterson & Wong, 2005), and
716 therefore may only be applicable to low porosity rocks, such as granite, before neighboring
717 fractures begin to perturb each other's local stress field. The present analysis suggests that future
718 work may benefit from considering data from a variety of rock types, including both sandstone
719 and granite, when deriving equations between the two- and three-dimensional properties.

720 4.3. Comparing complex machine learning algorithms to simple algorithms and statistics

721 Consistent with the performance of the gradient boosting models (**Figure 4**), and the
722 correlation coefficients between the two- and three-dimensional porosity, and fracture area and
723 volume (**Figure S6**), linear regression models are able to perform with moderate-strong
724 correlations between the observed and predicted values (**Figure 6a-b**). The strong performance
725 of these models allowed close examination of the coefficients of the models (**Figure 7**, **Figure**
726 **9**), which help provide constraints on equations that relate the three-dimensional and two-
727 dimensional properties. For models that predict the porosity with R^2 scores greater than 0.7, the
728 range of the value of the coefficients (**Figure S8**) suggests that the horizontal slices of rock cores
729 tend to overestimate the three-dimensional porosity as they require coefficients less than one. In
730 contrast, the vertical slices can provide a close approximation of the three-dimensional porosity,
731 requiring coefficients close to one. One explanation for this stronger correlation could be that the
732 presence of vertically-trending fractures produces larger porosities and areas measured along the
733 vertical orientation. However, measuring the orientation of individual fractures in a subset of
734 these experiments, which includes all but the sandstone experiments, does not reveal a clear
735 preferred orientation of the fractures (McBeck et al., 2022). The preferred explanation of this
736 result is that the vertical slices provide more information about the system than the horizontal
737 slices because they sample a larger area. Indeed, when the models only have access to one slice,
738 the models developed with one vertical slice perform better than the models developed with one
739 horizontal slice (e.g., **Figure 5a-b**) when they predict the volume and porosity using data from all
740 of the rock types.

741 Examining the coefficients of the linear regression models that predict the volume of the
742 largest fracture reveals that the complex geometry of the largest fractures produces a discrepancy
743 between the mathematically-expected relationship between the fracture area and volume, and the
744 coefficients determined from machine learning (**Text S2**). **Text S2** describes the derivation of the
745 value of the coefficients expected from the intersection of a plane with ellipsoids of varying
746 shape anisotropy. The geometric complexity of the large, system-spanning fractures can cause
747 the most volumetric fracture identified in the entire three-dimensional system to not be the
748 largest fracture, with the highest area, identified in a particular two-dimensional slice. The
749 machine learning models then must use the area of the largest fracture identified in a particular
750 slice to predict the volume of the largest fracture found throughout the system, which may not be
751 the same fracture. The high values of the coefficients highlight that accurate estimates of the
752 volume of the largest fracture in a three-dimensional system from two-dimensional

753 measurements of the area require a larger multiplicative factor than expected mathematically
754 from the intersection of a plane with an ellipsoid.

755 Due to the strong performance of the linear regression models and strong correlations
756 between the mean of the two-dimensional porosity measurements and three-dimensional values
757 (**Figure 9a-c**), we examined the ability of simple statistics to estimate the three-dimensional
758 porosity. For the rocks with the most isotropic and homogeneous fracture networks (sandstone),
759 calculating the mean of the two-dimensional measurements requires about the same number of
760 slices for successful estimates as the gradient boosting models, and a lower number of slices
761 compared to the linear regression models (**Figure 9d**). However, for the more heterogeneous
762 rocks (granite, monzonite, marble), the gradient boosting models require a lower number of
763 slices, and the linear regression models require the same or a lower number of slices than
764 calculating the mean for all of the rocks.

765 The homogeneous pore and fracture networks of the sandstone thus enable simple
766 statistics to provide more accurate estimates of the three-dimensional property than the linear
767 regression models, and similarly accurate estimates as the gradient boosting models, for the same
768 amount of data. This result is consistent with previous work that estimated the three-dimensional
769 permeability using two-dimensional measurements in sandstone with success, but was not able to
770 derive accurate estimates in more heterogeneous carbonate rocks (Saxena et al., 2017). The
771 heterogeneity of the fracture and pore network controls the potential accuracy of estimates of the
772 three-dimensional property because a random two-dimensional slice will likely be less
773 representative of the full three-dimensional system in a heterogeneous rock compared to a
774 homogeneous rock. Thus, homogeneous and heterogeneous rocks may require different
775 approaches to approximating the influence of fracture networks on fluid flow. An equivalent
776 porous medium approach, in which representative elementary volumes approximate the
777 distribution of hydrogeologic properties (e.g., Shaik et al., 2011), may be appropriate for
778 homogeneous rock. In contrast, such continuum approaches may not be appropriate for more
779 heterogeneous rocks, which instead may require modelling with a discrete fracture network (e.g.,
780 Cacas et al., 1990). In this type of modelling, a population of fractures is stochastically generated
781 using probability density functions that determine their geometric properties, including lengths,
782 apertures, and orientations (e.g., Lei et al., 2017). Previous work has used observations of natural
783 fracture networks to build two-dimensional models with discrete fracture networks (e.g.,
784 Belayneh & Cosgrove, 2004). However, because there is no established method of extrapolating
785 fracture geometries from two- to three-dimensions, few studies have extended such natural
786 observations into a three-dimensional discrete fracture network model (Lei et al., 2017). The
787 present analysis provides insight into how to robustly perform this extrapolation.

788 Similar to the apparent effectiveness of continuum approaches for the homogeneous
789 rocks (e.g., **Figure 9d**), models developed with all of the rock types to predict the porosity using
790 a set of statistics of the two-dimensional measurements primarily depend on the mean and
791 median (**Figure 10**). However, the models that predict the volume and tortuosity of the largest
792 fracture do not strongly depend on the mean, and instead depend primarily on the minimum area,
793 or minimum tortuosity, of the largest fracture identified in the group of two-dimensional slices.
794 The minimum values may be the most useful to the model predictions because they control the
795 ability of the fracture network to achieve the percolation threshold, when the fracture network
796 traverses the system. Indeed, in synthetic isotropic fracture networks with power law size-

797 distributed fractures near the percolation threshold, the two-dimensional permeability tends to
798 underestimate the three-dimensional permeability by three orders of magnitude (Lang et al.,
799 2014). Percolation thus may occur in three-dimensions, but not in two-dimensions when the
800 fracture density is low (Lang et al., 2014). Consequently, the minimum value of the fracture area
801 and tortuosity measured in two-dimensions should have a significant impact on the overall three-
802 dimensional volume and tortuosity. Thus, efforts to predict the geometry and resulting
803 connectivity of the largest fracture in a system should focus on the smallest values in a
804 population of two-dimensional observations rather than the mean or maximum values.

805 **5 Conclusions**

806 Data from eleven in situ X-ray tomography experiments during triaxial deformation
807 provide unique insights into the relationship between two- and three-dimensional measurements
808 of properties that control fluid flow in both homogeneous and heterogeneous rocks subjected to
809 differential stress loading until macroscopic failure. The machine learning models that predict
810 the porosity and volume of the largest fracture perform with strong correlations between the
811 predicted and observed values, and better than models that predict the tortuosity of the largest
812 fracture. This result highlights the difficulty of successfully estimating the tortuosity, and related
813 properties such as the permeability, from two-dimensional measurements or simulations, but
814 suggests that two-dimensional approaches may provide robust insights for analyses that focus
815 only on the volume of the largest fracture or porosity.

816 The analysis enables close examination of the amount and type of two-dimensional data
817 required for successful estimates of the three-dimensional property. The models presented here
818 can achieve accurate estimates of the porosity and volume of the largest fracture using only one
819 to four two-dimensional slices. Moreover, the method of slice extraction does not systematically
820 influence the model performance. In addition, models developed using data from all of the
821 experiments perform better than models developed for individual rock types. Consequently,
822 based on our dataset of triaxial compression experiments: 1) dense sampling of the subsurface or
823 rock core may not be required for successful estimates of some three-dimensional properties
824 (porosity, fracture volume); 2) the orientation of field measurements may not exert a significant
825 control on estimates of the three-dimensional property; and 3) including data from a variety of
826 rock types may lead to more successful estimates of the three-dimensional property than only
827 focusing on one rock type, in contrast to previous work that developed separate failure criteria
828 for separate rock types (e.g., Zhang et al., 1990; Paterson & Wong, 2005).

829 Comparing the amount of data required for more complex machine learning algorithms
830 (gradient boosting) to estimate the porosity to the amount required for simple statistics highlights
831 the benefit of machine learning for heterogeneous rocks. When rocks contain homogeneous and
832 isotropic pore and fracture networks, calculating the mean of the two-dimensional slices requires
833 a similar amount of data to successfully estimate the three-dimensional values as the gradient
834 boosting models, and less data than the linear regression models. Similarly, models developed
835 using a set of statistics of the two-dimensional measurements of all of the rock types indicate that
836 the mean and median of the two-dimensional value provide the most useful information when the
837 models predict the porosity. These results suggest that equivalent porous medium approaches
838 (e.g., Shaik et al., 2011) may be appropriate for homogeneous rocks, such as sandstone.
839 However, when the models predict the tortuosity and volume of the largest fracture, the models

840 primarily depend on the minimum value of the two-dimensional measurement in a set of slices.
 841 Thus, efforts to reconstruct the geometry and connectivity of the largest fracture in a system
 842 should focus on the smallest values in a population of local two-dimensional observations, rather
 843 than the mean. Heterogeneous rocks that include fracture populations with a wide range of
 844 lengths may require modelling using discrete fracture networks (e.g., Lei et al., 2017), rather than
 845 continuum approaches.

846 **Acknowledgments**

847 The study was funded by the Norwegian Research Council (grant 300435 to JM), UNINETT
 848 Sigma2 AS (project NN9806K), and the European Research Council (ERC) under the European
 849 Union's Horizon 2020 research and innovation program (grant agreement No. 101019628
 850 BREAK to FR). The experimental data is available on the Sigma2/NIRD/Norstore repository
 851 (Renard, 2017, 2018, 2021).

852 **References**

- 853 Auradou, H., Drazer, G., Hulin, J. P., & Koplik, J. (2005). Permeability anisotropy induced by
 854 the shear displacement of rough fracture walls. *Water Resources Research*, 41(9).
- 855 Bakke, S., & Øren, P. E. (1997). 3-D pore-scale modelling of sandstones and flow simulations in
 856 the pore networks. *SPE Journal*, 2(02), 136-149.
- 857 Bear, J. (1988) Dynamics of fluids in porous media. Elsevier, New York.
- 858 Belayneh, M., & Cosgrove, J. W. (2004). Fracture-pattern variations around a major fold and
 859 their implications regarding fracture prediction using limited data: an example from the Bristol
 860 Channel Basin. *Geological Society, London, Special Publications*, 231(1), 89-102.
- 861 Bobet, A., & Einstein, H. H. (1998). Fracture coalescence in rock-type materials under uniaxial
 862 and biaxial compression. *International Journal of Rock Mechanics and Mining Sciences*, 35(7),
 863 863-888.
- 864 Buades, A., Coll, B., & Morel, J. M. (2005). A non-local algorithm for image denoising. *IEEE*
 865 *Computer Society Conference on Computer Vision and Pattern Recognition (CVPR'05)* (Vol. 2,
 866 pp. 60-65). IEEE.
- 867 Bultreys, T., De Boever, W., & Cnudde, V. (2016). Imaging and image-based fluid transport
 868 modeling at the pore scale in geological materials: A practical introduction to the current state-
 869 of-the-art. *Earth-Science Reviews*, 155, 93-128.
- 870 Bühlmann, P., & Yu, B. (2003). Boosting with the L2 loss: regression and classification. *Journal*
 871 *of the American Statistical Association*, 98(462), 324-339.
- 872 Cacas, M. C., Ledoux, E., de Marsily, G., Tillie, B., Barbreau, A., Durand, E., ... & Peaudecerf,
 873 P. (1990). Modeling fracture flow with a stochastic discrete fracture network: calibration and
 874 validation: 1. The flow model. *Water Resources Research*, 26(3), 479-489.
- 875 Cao, R., Yao, R., Meng, J., Lin, Q., Lin, H., & Li, S. (2020). Failure mechanism of non-
 876 persistent jointed rock-like specimens under uniaxial loading: laboratory testing. *International*
 877 *Journal of Rock Mechanics and Mining Sciences*, 132, 104341.

- 878 Caumon, G., Collon-Drouaillet, P. L. C. D., Le Carlier de Veslud, C., Viseur, S., & Sausse, J.
879 (2009). Surface-based 3D modeling of geological structures. *Mathematical Geosciences*, 41(8),
880 927-945.
- 881 Chen, T., & Guestrin, C. (2016). XGBoost: A scalable tree boosting system. *Proceedings of the*
882 *22nd ACM SIGKDD international conference on knowledge discovery and data mining*, 785-
883 794.
- 884 Dominguez, S., Malavieille, J., & Lallemand, S. E. (2000). Deformation of accretionary wedges
885 in response to seamount subduction: Insights from sandbox experiments. *Tectonics*, 19(1), 182-
886 196.
- 887 Dong, H., & Blunt, M. J. (2009). Pore-network extraction from micro-computerized-tomography
888 images. *Physical Review E*, 80(3), 036307.
- 889 Duda, A., Koza, Z., & Matyka, M. (2011). Hydraulic tortuosity in arbitrary porous media flow.
890 *Physical Review E*, 84(3), 036319.
- 891 Elmorsy, M., El-Dakhkhni, W., & Zhao, B. (2022). Generalizable Permeability Prediction of
892 Digital Porous Media via a Novel Multi-scale 3D Convolutional Neural Network. *Water*
893 *Resources Research*, e2021WR031454.
- 894 Esmailpour, M., Ghanbarian, B., Liang, F., & Liu, H. H. (2021). Scale-dependent permeability
895 and formation factor in porous media: Applications of percolation theory. *Fuel*, 301, 121090.
- 896 Friedman, J. H. (2001). Greedy function approximation: a gradient boosting machine. *Annals of*
897 *Statistics*, 29(5), 1189-1232.
- 898 Ghanbarian, B. (2022). Estimating the scale dependence of permeability at pore and core scales:
899 Incorporating effects of porosity and finite size. *Advances in Water Resources*, 104123.
- 900 Gueting, N., Caers, J., Comunian, A., Vanderborght, J., & Englert, A. (2018). Reconstruction of
901 three-dimensional aquifer heterogeneity from two-dimensional geophysical data. *Mathematical*
902 *Geosciences*, 50(1), 53-75.
- 903 Hazlett, R. D. (1997). Statistical characterization and stochastic modeling of pore networks in
904 relation to fluid flow. *Mathematical Geology*, 29(6), 801-822.
- 905 Iding, M., & Ringrose, P. (2010). Evaluating the impact of fractures on the performance of the In
906 Salah CO2 storage site. *International Journal of Greenhouse Gas Control*, 4(2), 242-248.
- 907 Kamrava, S., Tahmasebi, P., & Sahimi, M. (2020). Linking morphology of porous media to their
908 macroscopic permeability by deep learning. *Transport in Porous Media*, 131(2), 427-448.
- 909 Karimpouli, S., & Tahmasebi, P. (2016). Conditional reconstruction: An alternative strategy in
910 digital rock physics. *Geophysics*, 81(4), D465-D477.
- 911 Karimpouli, S., Tahmasebi, P., & Saenger, E. H. (2018). Estimating 3D elastic moduli of rock
912 from 2D thin-section images using differential effective medium theory. *Geophysics*, 83(4),
913 MR211-MR219.
- 914 Keehm, Y., Mukerji, T., & Nur, A. (2004). Permeability prediction from thin sections: 3D
915 reconstruction and Lattice-Boltzmann flow simulation. *Geophysical Research Letters*, 31(4).

- 916 Kozłowska, M., Brudzinski, M. R., Friberg, P., Skoumal, R. J., Baxter, N. D., & Currie, B. S.
917 (2018). Maturity of nearby faults influences seismic hazard from hydraulic fracturing.
918 *Proceedings of the National Academy of Sciences*, 115(8), E1720-E1729.
- 919 Lang, P. S., Paluszny, A., & Zimmerman, R. W. (2014). Permeability tensor of three-
920 dimensional fractured porous rock and a comparison to trace map predictions. *Journal of*
921 *Geophysical Research: Solid Earth*, 119(8), 6288-6307.
- 922 Lei, Q., Latham, J. P., Tsang, C. F., Xiang, J., & Lang, P. (2015). A new approach to upscaling
923 fracture network models while preserving geostatistical and geomechanical characteristics.
924 *Journal of Geophysical Research: Solid Earth*, 120(7), 4784-4807.
- 925 Lei, Q., Latham, J. P., & Tsang, C. F. (2017). The use of discrete fracture networks for modelling
926 coupled geomechanical and hydrological behaviour of fractured rocks. *Computers and*
927 *Geotechnics*, 85, 151-176.
- 928 Li, Y., LeBoeuf, E. J., Basu, P. K., & Mahadevan, S. (2005). Stochastic modeling of the
929 permeability of randomly generated porous media. *Advances in Water Resources*, 28(8), 835-
930 844.
- 931 Luhmann, A. J., Tutolo, B. M., Bagley, B. C., Mildner, D. F., Seyfried Jr, W. E., & Saar, M. O.
932 (2017). Permeability, porosity, and mineral surface area changes in basalt cores induced by
933 reactive transport of CO₂-rich brine. *Water Resources Research*, 53(3), 1908-1927.
- 934 Lundberg, S. M., & Lee, S. I. (2017). A unified approach to interpreting model predictions.
935 *Advances in Neural Information Processing Systems*, 4765-4774.
- 936 Manwart, C., & Hilfer, R. (1999). Reconstruction of random media using Monte Carlo methods.
937 *Physical Review E*, 59(5), 5596.
- 938 Manwart, C., Torquato, S., & Hilfer, R. (2000). Stochastic reconstruction of sandstones. *Physical*
939 *Review E*, 62(1), 893
- 940 Marafini, E., La Rocca, M., Fiori, A., Battiato, I., & Prestininzi, P. (2020). Suitability of 2D
941 modelling to evaluate flow properties in 3D porous media. *Transport in Porous Media*, 134(2),
942 315-329.
- 943 McBeck, J., Aiken, J. M., Cordonnier, B., Ben-Zion, Y., & Renard, F. (2022). Predicting fracture
944 network development in crystalline rocks. *Pure and Applied Geophysics*, 179(1), 275-299.
- 945 McBeck, J. A., Cordonnier, B., & Renard, F. (2021). The influence of spatial resolution and
946 noise on fracture network properties calculated from X-ray microtomography data. *International*
947 *Journal of Rock Mechanics and Mining Sciences*, 147, 104922.
- 948 Mitchell, T. M., & Faulkner, D. R. (2012). Towards quantifying the matrix permeability of fault
949 damage zones in low porosity rocks. *Earth and Planetary Science Letters*, 339, 24-31
- 950 Moore, G. F., Shipley, T. H., Stoffa, P. L., Karig, D. E., Taira, A., Kuramoto, S., Tokuyama, H.,
951 & Suyehiro, K. (1990). Structure of the Nankai Trough accretionary zone from multichannel
952 seismic reflection data. *Journal of Geophysical Research: Solid Earth*, 95(B6), 8753-8765.
- 953 Mostaghimi, P., Blunt, M. J., & Bijeljic, B. (2013). Computations of absolute permeability on
954 micro-CT images. *Mathematical Geosciences*, 45(1), 103-125.

- 955 Nordahl, K., & Ringrose, P. S. (2008). Identifying the representative elementary volume for
956 permeability in heterolithic deposits using numerical rock models. *Mathematical Geosciences*,
957 40(7), 753-771.
- 958 Paterson, M. S., & Wong, T. F. (2005). Experimental rock deformation-the brittle field. *Springer*
959 *Science & Business Media*.
- 960 Pedregosa, F., Varoquaux, G., Gramfort, A., Michel, V., Thirion, B., Grisel, O., Blondel, M.,
961 Prettenhofer, P., Weiss, R., Dubourg, V., Vanderplass, J., Passos, A., Cournapeau, D., Brucher,
962 M., Perrot, M., & Duchesnay, E. (2011). Scikit-learn: Machine learning in Python. *The Journal*
963 *of Machine Learning Research*, 12, 2825-2830.
- 964 Raghavan, R. (2006). Some observations on the scale dependence of permeability by pumping
965 tests. *Water Resources Research*, 42(7)
- 966 Renard, F. (2017). Critical evolution of damage towards system size failure in a crystalline rock
967 [Data set]. Norstore. doi:10.11582/2017.00025.
- 968 Renard, F. (2018). Volumetric and shear processes in crystalline rock during the approach to
969 faulting [Data set]. Norstore. doi:10.11582/2018.00023.
- 970 Renard, F. (2021). X-ray tomography data of Westerley granite [Data set]. Norstore.
971 doi:10.11582/2021.00002.
- 972 Renard, F., Cordonnier, B., Dysthe, D. K., Boller, E., Tafforeau, P., & Rack, A. (2016). A
973 deformation rig for synchrotron microtomography studies of geomaterials under conditions down
974 to 10 km depth in the Earth. *Journal of Synchrotron Radiation*, 23(4), 1030-1034.
- 975 Renard, F., McBeck, J., Cordonnier, B., Zheng, X., Kandula, N., Sanchez, J. R., & Dysthe, D. K.
976 (2019). Dynamic in situ three-dimensional imaging and digital volume correlation analysis to
977 quantify strain localization and fracture coalescence in sandstone. *Pure and Applied Geophysics*,
978 176(3), 1083-1115.
- 979 Renard, F., Weiss, J., Mathiesen, J., Ben-Zion, Y., Kandula, N., & Cordonnier, B. (2018).
980 Critical evolution of damage toward system-size failure in crystalline rock. *Journal of*
981 *Geophysical Research: Solid Earth*, 123(2), 1969-1986.
- 982 Roberts, A. P. (1997). Statistical reconstruction of three-dimensional porous media from two-
983 dimensional images. *Physical Review E*, 56(3), 3203.
- 984 Rovey, C. W., & Cherkauer, D. S. (1995). Scale dependency of hydraulic conductivity
985 measurements. *Groundwater*, 33(5), 769-780.
- 986 Rutter, E. H. (1972). The influence of interstitial water on the rheological behaviour of calcite
987 rocks. *Tectonophysics*, 14(1), 13-33.
- 988 Sahimi, M., Hughes, B. D., Scriven, L. E., & Davis, H. T. (1986). Dispersion in flow through
989 porous media—I. One-phase flow. *Chemical Engineering Science*, 41(8), 2103-2122.
- 990 Santos, J. E., Xu, D., Jo, H., Landry, C. J., Prodanović, M., & Pyrcz, M. J. (2020). PoreFlow-
991 Net: A 3D convolutional neural network to predict fluid flow through porous media. *Advances in*
992 *Water Resources*, 138, 103539.
- 993 Sánchez-Vila, X., Carrera, J., & Girardi, J. P. (1996). Scale effects in transmissivity. *Journal of*
994 *Hydrology*, 183(1-2), 1-22.

- 995 Sassi, W., Colletta, B., Balé, P., & Paquereau, T. (1993). Modelling of structural complexity in
 996 sedimentary basins: the role of pre-existing faults in thrust tectonics. *Tectonophysics*, 226(1-4),
 997 97-112.
- 998 Saxena, N., & Mavko, G. (2016). Estimating elastic moduli of rocks from thin sections: Digital
 999 rock study of 3D properties from 2D images. *Computers & Geosciences*, 88, 9-21.
- 1000 Saxena, N., Mavko, G., Hofmann, R., & Srisutthiyakorn, N. (2017). Estimating permeability
 1001 from thin sections without reconstruction: Digital rock study of 3D properties from 2D images.
 1002 *Computers & Geosciences*, 102, 79-99.
- 1003 Schulze-Makuch, D., Carlson, D. A., Cherkauer, D. S., & Malik, P. (1999). Scale dependency of
 1004 hydraulic conductivity in heterogeneous media. *Groundwater*, 37(6), 904-919.
- 1005 Shaik, A. R., Rahman, S. S., Tran, N. H., & Tran, T. (2011). Numerical simulation of fluid-rock
 1006 coupling heat transfer in naturally fractured geothermal system. *Applied Thermal Engineering*,
 1007 31(10), 1600-1606.
- 1008 Sudakov, O., Burnaev, E., & Koroteev, D. (2019). Driving digital rock towards machine
 1009 learning: Predicting permeability with gradient boosting and deep neural networks.
 1010 *Computational Geosciences*, 127, 91-98.
- 1011 Tian, J., Qi, C., Sun, Y., Yaseen, Z. M., & Pham, B. T. (2021). Permeability prediction of porous
 1012 media using a combination of computational fluid dynamics and hybrid machine learning
 1013 methods. *Engineering with Computers*, 37(4), 3455-3471.
- 1014 Tong, H., Koyi, H., Huang, S., & Zhao, H. (2014). The effect of multiple pre-existing
 1015 weaknesses on formation and evolution of faults in extended sandbox models. *Tectonophysics*,
 1016 626, 197-212.
- 1017 Wei, T., Fan, W., Yu, N., & Wei, Y. N. (2019). Three-dimensional microstructure
 1018 characterization of loess based on a serial sectioning technique. *Engineering Geology*, 261,
 1019 105265.
- 1020 Wilshaw, T. R. (1971). The Hertzian fracture test. *Journal of Physics D: Applied Physics*, 4(10),
 1021 1567.
- 1022 Yeong, C. L. Y., & Torquato, S. (1998). Reconstructing random media. *Physical Review E*,
 1023 57(1), 495.
- 1024 Zhang, J., Wong, T. F., & Davis, D. M. (1990). Micromechanics of pressure-induced grain
 1025 crushing in porous rocks. *Journal of Geophysical Research: Solid Earth*, 95(B1), 341-352.
- 1026 Zhang, D., Zhang, R., Chen, S., & Soll, W. E. (2000). Pore scale study of flow in porous media:
 1027 Scale dependency, REV, and statistical REV. *Geophysical Research Letters*, 27(8), 1195-1198.
- 1028 Øren, P. E., & Bakke, S. (2002). Process based reconstruction of sandstones and prediction of
 1029 transport properties. *Transport in Porous Media*, 46(2), 311-343.
- 1030 Øren, P. E., & Bakke, S. (2003). Reconstruction of Berea sandstone and pore-scale modelling of
 1031 wettability effects. *Journal of Petroleum Science and Engineering*, 39(3-4), 177-199.